

Deep Generative Modeling for Volume Reconstruction in Cryo-Electron Microscopy

Claire Donnat¹, Axel Levy^{2,3}, Frédéric Poitevin³, and Nina Miolane⁴

¹University of Chicago, Department of Statistics, Chicago, Illinois, USA

²Stanford University, Department of Electrical Engineering, Stanford, CA, USA

³Department of LCLS Data Analytics, SLAC National Accelerator Laboratory, Menlo Park, CA, USA

⁴University of California Santa Barbara, Department of Electrical and Computer Engineering, Santa Barbara, CA, USA

*ninamiolane@ucsb.edu

ABSTRACT

Recent breakthroughs in high resolution imaging of biomolecules in solution with cryo-electron microscopy (cryo-EM) have unlocked new doors for the reconstruction of molecular volumes, thereby promising further advances in biology, chemistry, and pharmacological research amongst others. Despite significant headway, the immense challenges in cryo-EM data analysis remain legion and intricately inter-disciplinary in nature, requiring insights from physicists, structural biologists, computer scientists, statisticians, and applied mathematicians. Meanwhile, recent next-generation volume reconstruction algorithms that combine generative modeling with end-to-end unsupervised deep learning techniques have shown promising results on simulated data, but still face considerable hurdles when applied to experimental cryo-EM images. In light of the proliferation of such methods and given the interdisciplinary nature of the task, we propose here a critical review of recent advances in the field of *deep generative modeling for high resolution cryo-EM volume reconstruction*. The present review aims to (i) compare and contrast these new methods, while (ii) presenting them from a perspective and using terminology familiar to scientists in each of the five aforementioned fields with no specific background in cryo-EM. The review begins with an introduction to the mathematical and computational challenges of *deep generative models for cryo-EM volume reconstruction*, along with an overview of the baseline methodology shared across this class of algorithms. Having established the common thread weaving through these different models, we then dive into the specifics and provide a practical comparison of these state-of-the-art algorithms, highlighting their relative strengths and weaknesses, along with the assumptions that they rely on. This allows us to identify bottlenecks in current methods and avenues for future research. This review might also raise the interest of computer vision practitioners, as it highlights current limits of deep generative models in a very challenging imaging regime where, for example, the signal-to-noise ratio is considerably lower than that found in traditional images.

Introduction

High resolution reconstruction of molecular volumes from [single particle images](#) has the potential to facilitate new breakthroughs in our ability to understand fundamental biological mechanisms and/or engineer macromolecular function^{2,1}. In this context, cryo-electron microscopy (**cryo-EM**) has fostered a revolution in structural biology by allowing the imaging of biological molecules in solution “frozen in time” from near-atomic to atomic resolution² (see EMDB³ for a visualization of the trend). However, observations of 3D molecules (also called **particles**) are limited to their raw 2D projections relative to an incoming electron beam, with no information on their 3D orientation or position — see Figure 1. The crux of the inverse reconstruction problem thus consists of simultaneously recovering the underlying molecular volumes along with a number of hidden variables such as the molecule’s 3D orientation or position at acquisition time. The reconstruction task, however, is made uniquely challenging by a combination of factors, including the variability in the shape of any given molecule (also referred to as “[conformational heterogeneity](#)”), the high number of unknown parameters that have to be imputed, the non-linear physics of the data acquisition process, as well as remarkably low signal-to-noise ratios. These concepts are formalized below, by introducing the image formation model.

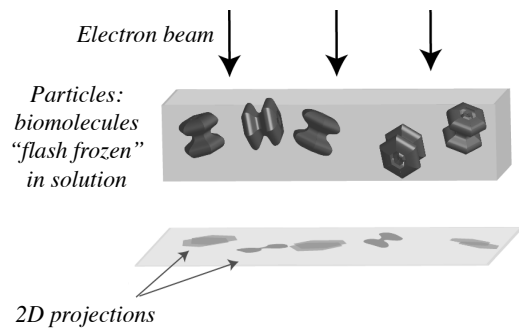


Figure 1. Acquisition of 2D cryo-EM images (2D projections) from 3D biomolecular volumes. The diagram shows an electron beam (three arrows) passing through a sample containing particles (biomolecules) “flash frozen” in solution. The particles are represented as 3D volumes. The resulting 2D projections are shown as a horizontal slice with several greyish, irregular shapes representing the 2D images of the 3D particles. The caption text describes the figure as illustrating the acquisition of 2D cryo-EM images from 3D biomolecular volumes, mentioning the electron beam, particles (biomolecules), and 2D projections.

Image Formation Model. The process of image formation in cryo-EM involves several complex physical phenomena: (i) pairwise interactions between atoms, (ii) the creation of an electrostatic potential from the charges carried by the molecule and its surrounding environment, (iii) the interaction between the probing electron beam and the electrostatic potential, and finally (iv) the effects of the lens system and detector on the recorded image. The interested reader can learn more in Dill *et al.*⁷, Kohl and Reimer⁴, and Vulovic *et al.*⁵. Nonetheless, in most cases^{5,6}, each image X_i of n single particles can be thought of as a random sample from the following generative model:

$$X_i = \text{PSF}_i * (t_i \circ \Pi_{2D} \circ R_i)(V^{(i)}) + \varepsilon_i, \quad \text{with } i = 1 \dots n. \quad (1)$$

Here, R_i is a 3D rotation representing the 3D orientation of the volume $V^{(i)}$ with respect to the direction of the electron beam. The oriented volume is subsequently “pierced through” by the electron beam and projected onto the detector — an operation represented in Equation (1) by the 2D-projection operator Π_{2D} . The variable t_i represents the 2D translation of the projected volume with respect to the centre of the image. The effect of the microscope’s lens system is modeled through the convolution $*$ of the 2D projection by an image-dependent operator PSF_i called the Point Spread Function (PSF) of the microscope whose parameters such as the defocus can be image dependent. Finally, additional noise is introduced in the observed image, as represented by the variable ε_i , which is typically assumed to be centered with variance σ_i^2 .

Fourier-Slice Theorem. An alternative (and often simpler) generative model can also be formulated via the Fourier equivalent of Equation (1). In Fourier Space, the convolution $*$ of the projected 2D volume by the PSF conveniently becomes an element-wise matrix multiplication \odot between the 2D Fourier transform of the projected image and that of the PSF. The latter is better known as the Contrast Transfer Function (CTF), with $\text{CTF}_i = \mathcal{F}(\text{PSF}_i)$, so that:

$$\tilde{X}_i = \text{CTF}_i \odot (P_i^{(R_i, t_i)} \circ \tilde{V}^{(i)}) + N_i, \quad \text{with } i = 1 \dots n. \quad (2)$$

Here, \tilde{X}_i is the 2D-Fourier transform of the observed image X_i ($\tilde{X}_i = \mathcal{F}(X_i)$), and $\tilde{V}^{(i)}$ is the 3D Fourier transform of the molecule (i.e., the volume) $V^{(i)}$, with $\tilde{V}_i = \mathcal{F}(V_i)$. In this equation, the operator $P_i^{(R_i, t_i)}$ first extracts out of $\tilde{V}^{(i)}$ a slice oriented by the rotation R_i and then applies a phase shift in Fourier space accounting for the 2D translation t_i . Finally, N_i represents the noise. We note that using the operator P_i circumvents the 3D-to-2D projection step and is therefore more efficient from a computational standpoint.

Statistical and Computational Challenges of Cryo-EM. Whether in Image or Fourier space, the image generation process described by Equations (1) and (2) gives us the first clue about the difficulty of the reconstruction problem. *Only the recovery of the 3D conformational landscape (in other words, the set of all possible conformations $V^{(i)}$ or $\tilde{V}^{(i)}$) is relevant.* All pose variables R_i , t_i and camera variables PSF_i (respectively CTF_i) in image (resp. Fourier) space are “nuisance” variables in the statistical sense. As put by Singer *et al.*⁷, while they have the potential to impact the quality of the reconstruction by scrambling the signal, they do not bring any information of biological relevance. Consequently, the cryo-EM reconstruction problem has to overcome three main hurdles:

(a) Scalability. Due to the number of unknown variables that have to be estimated (i.e. the individual volumes $V^{(i)}$ and nuisance variables R_i , t_i , PSF_i), algorithms often struggle to process the wealth of incoming images⁸, to the point where “the cost of image analysis can exceed 500,000 CPU hours on large, expensive computer clusters”⁹ for a single experiment.

(b) Robustness to noise. Recent developments in unsupervised deep learning have opened the door to significant speed-ups in computation through the use of gradient methods and GPUs. However, despite promising results on simulated datasets, these methods face considerable challenges when applied to real cryo-EM images, which are characterised by much lower signal-to-noise regimes. These algorithms have not been properly vetted and stress-tested in experimental conditions.

(c) Robustness to initial conditions. The high number of unknown variables hinders the robustness of reconstruction methods. In this setting, the reconstruction challenge becomes a highly non-convex optimization problem with many local minima. Consequently, reconstruction methods become sensitive to initialization¹⁰ and run the risk of converging to local minima¹¹. Together, these three hurdles mean that inference for cryo-EM reconstruction is an immensely challenging and very active area of research, both from computational and a statistical perspective.

Related Work. With the booming interest for cryo-EM methods, there already exists a number of reviews, each focusing on various angles of the cryo-EM reconstruction problem. The reviews by Bendory *et al.*¹² and Singer *et al.*⁷ provide an extremely complete overview of the field, including the physics of the imaging process and the multiple stages of the reconstruction pipelines. However, these reviews focus on general computational methods and their mathematical foundations, but with no particular focus on deep learning. These methods in fact predate most of the deep modeling methods described in the present review. The closest work to ours is perhaps the review presented by Si *et al.*¹³, which describes the impact of artificial intelligence and deep learning on computational methods in cryo-EM. However, with the exception of cryoDRGN (Zhong *et al.*, 2019¹⁴), this review does not include the latest deep generative modeling methods. In the survey by Ede *et al.*¹⁵, the role of deep learning in electron microscopy is reviewed in introduction in relation to problems of denoising, classification (labelling) and segmentation. While this last review presents deep generative modeling and describes various architectures for

autoencoders, variational autoencoders, and generative adversarial networks, the associated sections are mostly expository, and none of the most recent deep generative modeling advances in cryo-EM are included. Finally, the review by Wu *et al.*¹⁶ provides an updated view compared to¹⁵ and includes a high-level description of the most recent deep generative modeling advances. By contrast, our review is a deep dive into the specifics of deep differentiable generative models specifically targeted to cryo-EM reconstruction. We emphasise here that such generative approaches are not the only way of performing cryo-EM volume reconstruction, and other approaches based on moment methods¹⁷ have been successfully applied to this problem as well. In this review, however, we limit our focus to candidate methods for high-resolution volume reconstruction, for which generative models have recently gained an increasing amount of traction in the community.

Our Objectives. We critically review recent cryo-EM reconstruction approaches leveraging deep generative modeling. Our review contrasts traditional generative methods with their new deep-learning based counterparts, while emphasizing the core statistical and computer science concepts behind each algorithm. We organize cryo-EM reconstruction pipelines according to (1) the parametrization of the reconstruction problem through generative models in Section 1 and (2) the inference tools deployed to invert these generative models in Section 2. While this review covers the statistical foundations for modern reconstruction methods in cryo-EM, it does not address other topics related to statistics such as validation metrics or connections with statistical thermodynamics. We leave these topics for future work.

1 Generative Modeling for Cryo-EM

The objective of cryo-EM imaging algorithms is to produce a 3D reconstruction of a given molecule from a dataset of images $\{X_i\}_{i=1\dots n}$, where each image corresponds to a “2D projection” of the molecule at a different (unknown) orientation and position (Figure 1). An additional fundamental hurdle to this objective lies in the fact that each molecule has its own (unknown) conformation or shape. Methods that account for this **conformational heterogeneity** are called **heterogeneous reconstruction methods**, and can typically aspire to higher resolution reconstructions often at the cost of more involved and expensive computations. Conversely, those that neglect this shape variability and choose to represent the conformational landscape as a unique molecular volume are usually referred to as **homogeneous reconstruction methods**.

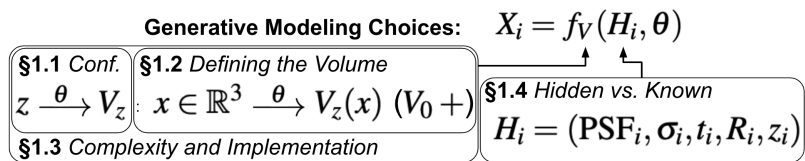


Figure 2. Graphical summary of Section 1, highlighting the possible choices in defining a generative model for cryo-EM. First, as detailed in Section 1.1, the conformational model needs to be chosen as being either discrete or continuous, through defining the conformation variable z . Second, as detailed in Section 1.2, the volume V needs to be defined. This entails defining its input domain as either a discrete grid or a continuous field that can either be represented implicitly with a neural network or as a mixture of Gaussian representing atomic coordinates. The output domain of V needs also to be defined, together with whether V represents a deviation from a reference or not. Section 1.3 discusses the consequences of these choices on the complexity of the model and its implementation. Finally, Section 1.4 discusses how certain hidden variables can be considered known instead and how the inference problem is setup as a consequence.

1.1 The Conformation Variable z .

Heterogeneous reconstruction methods introduce an additional variable z_i for each image i within the formation model of Equations (1) and (2), which we call the conformation variable. Depending on whether shape heterogeneity is modeled through a discrete number of states or as a continuous variable, the conformational landscape can be encoded as a discrete family of volumes $\mathcal{V} = \{V_z, z \in \{1, \dots, K\}\}$ (**discrete heterogeneity**), or as a continuous family $\mathcal{V} = \{V(z), z \in \mathbb{R}^L\}$ (**continuous heterogeneity**). In both cases, the family is parametrized by a variable z that encodes information about a molecule’s specific conformation. We use the notations V_z and $V(z)$ interchangeably. Note that homogeneous reconstruction can be taken as a special case of this parametrization, in which case \mathcal{V} only comprises a single volume, and $K = 1$ or $L = 0$. We can now write $V^{(i)} = V(z_i)$ in Equation (1) and $\tilde{V}^{(i)} = \tilde{V}(z_i)$ in Equation (2).

Interpretation of the Conformation Variable The conformation variable z_i permits storing information about the specific location of **particles** on the conformational landscape. For example, if $z_i \in \mathbb{R}$, z_i can be used to sort conformations along what would look like a molecule movie. Note that the dimensionality L of z could in principle take any value between 0 and on the order of the number of atoms in the molecule. However, two factors tend to drastically limit the number of dimensions of z . First, most of the main and global dynamics of a molecule are captured by a few **collective variables** associated with its low-frequency motion, effectively averaging out a lot of the effect of the high number of degrees of freedom associated with faster motions. Second, imaging conditions often reduce the ability to resolve the remaining motions, thus reducing the effective dimensionality of z . In other words, the limits of the imaging technology itself prevent us from aspiring to too

high-dimensional z . In the case of discrete heterogeneity, the conformation variable can be intuitively understood as an index of the minimum energy wells in the conformational landscape, and in this case too, imaging conditions reduce the ability to resolve too many metastable states.

Discrete Conformational Heterogeneity: Pros and Cons. Discrete heterogeneity has a rich history in cryo-EM. Popularized by RELION¹⁸ -Class3D^{6,19}, it offers the advantage of delivering readily interpretable results: a set of 3D volumes, representing the centroids of K main clusters of conformations. One of the main drawbacks of this method consists in the necessary selection of the number K of appropriate clusters. Theoretically, this could be done by cross-validating the results of multiple classification rounds. In practice, because of the computing toll of running such expensive calculations multiple times, K is chosen in an ad hoc fashion by the experimenter and rarely motivated by strong quantitative arguments. An alternative to cross-validation would be to leverage dimensionality reduction methods such as 3DVA²⁰ where cross-validation of clustering results is much less expensive and can be used to determine a number of appropriate clusters. Such dimensionality reduction methods allow the visualization of a more continuous distribution of conformations.

Continuous Conformational Heterogeneity: Pros and Cons. Consequently, many recent methods have turned to a continuous representation of heterogeneity which does not require specifying an appropriate number of clusters. This representation is also often deemed to be closer to the underlying biology, as molecules do not exist as finite/discrete sets of shapes. Rather, a more realistic analogy is to think of molecules as random samples from the equilibrium distribution over their conformational space. Table 1 shows that the majority of current heterogeneous reconstruction methods choose this approach. However, while a continuous representation is more relevant, it remains to be determined how accurate the reconstruction of the conformational space by the space indexed by z truly is. This latter point will be critical to address for heterogeneous reconstruction methods to become more quantitative and directly comparable to other measures from biophysicists and biochemists.

1.2 Defining the volume $V(z)$

We have formulated the cryo-EM reconstruction problem as the recovery of the underlying [conformational landscape](#). We now turn to the problem of finding a parametrization for each volume $V(z)$ of the conformational landscape \mathcal{V} . This requires choosing first, a space (image space vs. Fourier space, inducing real vs complex values), and second, an encoding style (reference-free vs. reference-based) for the volume representation.

1.2.1 Defining the output domain

As explained in the introduction, the image formation model can be described equivalently in image space or Fourier space. Thus, each volume within the family of possible conformations \mathcal{V} can be described either in terms of its image pixel intensities or its Fourier coefficients. In either case, the volume $V(z)$ associated with a specific conformation variable z is defined on a domain $\Omega \subset \mathbb{R}^3$ (the space of coordinates) and takes its values either in \mathbb{R} , where values represent image pixel intensities, or in \mathbb{C} , where values represent the amplitude and phase of the Fourier coefficients. From a practical standpoint, the choice of one space vs. another is typically guided by the set of properties and constraints that the analyst wishes to use to guide volume inference. Historically, the Fourier approach has been the preferred approach, due in part to the ease with which the slicing, rotation and translation operators can be accounted for in the image generation model (see discussion of Equation 2). As summarized by Punjani et al²¹, working in Fourier space thus has the benefits of (a) reducing the computational cost of CTF modulation and image projection, and (b) allowing closed-form Maximum likelihood reconstructions when the poses are known. However, recent methods such as 3DFlex²¹ have favored parametrization in image space, where constraints are more interpretable and where operations such as rotation, shifting and deformations of the molecule's density map are more naturally parameterized. Parametrization and constraining reconstruction in image space can thus be considered as a promising avenue for future development in cryo-EM volume reconstruction.

1.2.2 Defining the origin

If a reference template molecular shape V_0 is known, one can choose to parametrize the conformation landscape through its deviation $\Delta V(z)$ from the reference conformation V_0 , such that $V(z) = V_0 + \Delta V(z)$ or $V(z)$ is represented as a deformation of V_0 , instead of directly maintaining a representation of $V(z)$. This approach has the advantage of naturally biasing the representation of V such that $\Delta V(z) = 0$ implies $V(z) = V_0$, which in turn, can yield better conformations given the complexity of the problem. The column "Reference Volume" of Table 1 highlights which methods use a reference-free or conversely, a reference-based volume representation. For instance, the method E2GMM²² first operates in a reference-free fashion, and learns a template conformation V_0 called the "neutral representation" which then serves as the reference template to further refine the reconstruction and account for conformational variability. In atomVAE¹⁰, Rosenbaum et al uses a V_0 called a "base conformation" described as a set of atom coordinates, obtained from an auxiliary method such as an homogeneous reconstruction or a set of atom coordinates predicted by AlphaFold. The method 3DFlex²¹ uses a reference volume V_0 , called a "canonical density" or "canonical 3D map". However, there, V_0 is not supposed known, it is learned together with the

conformational heterogeneity. From a practical standpoint, whether to choose a reference-free or reference-based method is guided by (a) the number of unknown variables, and (b) the reliability of available reference models. When poses are unknown, and even further, when accounting for conformation heterogeneity, Cryo-EM volume reconstruction is a difficult, highly non-convex inference problem. As such, biasing the solution towards a reference one can provide an interesting way of ensuring a more reliable and consistent solution. Depending on the optimization pipeline used, this can in fact be critical to the success of the pipeline: Rosenbaum et al¹⁰ for instance report that adopting a reference-template and warm-starting their algorithm is essential to ensure the recovery of good conformations. However, there is a strong push in the community for methods able to operate in a reference-free setting, with three out of six current heterogeneous methods allowing to recover methods with no prior template (see Table 1). The development of methods able to recover volumes without any prior on the shape of the solution therefore seem to be an area of focus and future development in the community.

1.2.3 Defining the input domain

The volume $V(z)$ represents a scalar 3D field (electrostatic potential) and is therefore always defined as a function from \mathbb{R}^3 to \mathbb{R} (or \mathbb{C}). We now describe the specifics of the parametrization of this volume and distinguish two cases: whether the volume is defined as a discretized field or as a continuous field.

Discretized Domain and Explicit 3D Map parametrization. Our first class of approaches models the electrostatic potential as a discrete 3D map. That is, the target of the reconstruction is the estimate of the electrostatic potential at every location (or in any voxel) of a discretized 3D-space. In this case, the function $V(z)$ is defined on a discretized subspace (a grid) of \mathbb{R}^3 , namely $\Omega = \{1, \dots, D\}^3$, where D represents the length of the 3D voxel grid or frequency grid. $V(z)$ is then explicitly parametrized by the values it takes on Ω . In a “vectorial” formalism, $V(z)$ can be seen as a set of voxels with their corresponding potential values or as a set of Fourier components with their corresponding amplitudes and phases: *i.e.* $V(z) \in \mathbb{R}^{D^3}$ or $\tilde{V}(z) \in \mathbb{C}^{D^3}$. In this case, the resolution of the reconstructed volume is fixed by the choice of the granularity of the grid. However, this formalism implies that $V(z)$ becomes an infinite-dimensional vector when it is represented continuously (see next paragraph). For this reason, we prefer to use the “functional” formalism, *i.e.* to define the volume $V(z)$ as a function (not as a vector), whether it is modeled as a discrete or continuous object. The discretized approach is the one adopted by methods like RELION¹⁸ -Refine3D and RELION¹⁸ -Class3D¹⁸ in Fourier space, and CryoPoseNet²³²³ or 3DFlex²¹²¹ in Image space:

- RELION¹⁸ -Class3D¹⁹ uses discrete conformational heterogeneity through K clusters and $z \in \{1, \dots, K\}$, in Fourier space with a reference-free encoding. As a result, each of the K volumes \tilde{V}_z is parametrized by its J 3D Fourier coefficients, where $J = D^3$. The target of inference is thus the coefficients $\tilde{V}_{j,k}$ for the volume corresponding to each of these K clusters, where $j = 1 \dots J$ indexes the Fourier coefficients, and k the K clusters. RELION¹⁸ -Refine3D is a homogeneous reconstruction method where the volume is a single parameter \tilde{V} independent of the image X_i .
- CryoPoseNet²³²³ does not consider conformational heterogeneity: it is a homogeneous reconstruction method, where the volume is a single parameter V independent of the image X_i . CryoPoseNet²³ operates in Image space, using a reference-free encoding, where the volume is represented as 3D map over a discrete domain, *i.e.* as a set of image intensities on the voxel grid: $V \in \mathbb{R}^{D^3}$.
- 3DFlex²¹ models conformational heterogeneity through a continuous conformation variable z , in Image space, with a reference-based encoding where the volume is represented as deviations from an initial template V_0 . Here, Punjani *et al.* propose learning a deformation field $U \in \mathbb{R}^{3D^3}$ with respect to the conformation V_0 , that is explicitly represented by the coefficients of its 3D vectors at each of the voxels of the discrete domain. Consequently, the function V writes: $V(z) = f(U(z), V_0)$, where f is a convection operator used to deform the volume V_0 based on U , and z is the conformation variable. The deformation flow U is parametrized through a neural network.

Continuous Domain. Other methods model the volume $V(z)$ as a continuous field, which means that they represent the volume as a function on a continuous domain (\mathbb{R}^3 or $[-0.5, 0.5]^3$). This domain is infinite, and one cannot explicitly maintain the values $V(z)$ takes on its domain. The solution is then to use a parametric definition for the function $V(z) \in \{V_\theta, \theta \in \Theta\}$. Each volume $V(z)$ is defined by its parameters $\theta \in \Theta$ where Θ is (a subspace of) a finite-dimensional space. Depending on whether these parameters have a physical meaning (*e.g.* centroids of pseudo-atoms) or not, we distinguish two types of parametrization:

- (i) **Implicit 3D Map parametrization with a Neural Network.** Some methods use neural networks to represent $V(z)$ as a (real or complex) function of a three-dimensional vector. The parameters of the representation — *i.e.* the weights of the neural network — do not have a physical meaning. CryoDRGN¹⁴¹⁴ introduces this framework using a Fourier-related

space and reference-free volume representation. Contrary to the discretized-domain approach, here, the resolution of the recovered volume can theoretically be as sharp as desired, as any coordinates of \mathbb{R}^3 can be fed to $V(z)$.

(ii) Volumes as (Pseudo-)Atom Coordinates. The second class of approaches guides and constrains the recovery of the molecular volume by directly modeling the source of the electrostatic potential: its individual atoms or pseudo-atoms. Indeed, at a granular level, the molecular volume can be approximated by a mixture of Gaussian functions (called scattering form factors⁴) of the form:

$$V_z(x) = \sum_{j=1}^N A_j \exp\left(-\frac{\|c_j - x\|^2}{2\sigma_j^2}\right), \quad (3)$$

where $x \in \mathbb{R}^3$ represents a 3D coordinate in real Image space, and $c_j \in \mathbb{R}^3$ are the 3D coordinates of the N individual atoms or pseudo-atoms. The parameters $A_j \in \mathbb{R}$ and $\sigma_j^2 \in \mathbb{R}$ describe how each (pseudo-)atom contributes to the electrostatic potential. In practice, these approaches always implement conformational heterogeneity, and do so through a continuous conformation variable $z \in \mathbb{R}^L$ that passes through a neural network to output c_j , and possibly A_j and σ_j . This approach also models V_z as a continuous field, as defined by Equation (3), but the parameters defining each volume (c_j , A_j and σ_j) now have a physical meaning. This approach is therefore a way to simplify the parametrization of $V(z)$, taking into account physical knowledge derived from an atomic model. Among this general class of methods, different works differ in the interpretation given to the variable c_j and in whether A_j , σ_j^2 are assumed to be known:

- **c_j as coordinates of “coarse-grained atoms”.** The c_j are coordinates of “coarse-grained atoms”, which are not explicitly mapped onto groups of atoms within the molecular structure. E2GMM²² introduces this approach and uses it in a reference-free encoding. The authors describe its benefits as (a) reducing the number of parameters to represent the molecule at any level of detail (in contrast with the grid-approaches) and (b) providing a natural way of modeling cryo-EM maps — which, as described in the introduction, are the projections of the electrostatic potential “blob” around each atom. In E2GMM²², Chen *et al.* use a conformation variable z that encodes the coefficients c_j, A_j, σ_j^2 that define V_z in Equation (3).
- **c_j as 3D coordinates of groups of atoms.** The c_j are interpreted as coordinates of “residues”, *i.e.* physical groups of atoms that constitute the molecular structure of proteins. CryoFold²⁴ relies on this approach in a reference-free encoding. The conformation variable z only encodes the coordinates c_j , while $A_j = A$ and $\sigma_j = \sigma$ are assumed known and fixed.
- **c_j as 3D coordinates of (pseudo)-atoms.** The c_j are coordinates of actual atoms that constitute the molecular structure of proteins, or potentially pseudo-atoms: *i.e.* a 3D position that does not exactly correspond to the actual atom but averages known positions of real atoms. In atomVAE¹⁰, Rosenbaum *et al* explore this approach, using a reference-based encoding. In other words, Rosenbaum *et al.* consider that a template molecular shape V_0 is given, with associated coordinates c_j that form a “base conformation”. The volume is here parametrized in terms of the deviations from that template, expressed as residuals, or small variations Δc_j corresponding to different conformations relative to this base conformation. In this work, the conformation variable z encodes the deviations Δc_j while $A_j = A$ and $\sigma_j = \sigma$ are assumed known and fixed.

Pseudo-Atomic Methods: Pros and Cons. Pseudo-atomic methods effectively add structure to the solution, by assuming that the data are a mixture of Gaussians. These methods are particularly powerful when operating in a reference-based fashion, *i.e.* with respect to a base conformation V_0 . The increasing availability of folded protein shapes — traditionally from the Protein Data Bank²⁵ and more recently through the advent of AlphaFold²⁶ — have indeed enabled access to such base conformations. Compared to reference-free approaches, this unlocks new doors for molecular reconstruction by allowing parametrizations that are more amenable to taking into account molecular physics and dynamics. Interestingly, the authors of atomVAE¹⁰ found that using a reference-based method with respect to some base conformation was critical: randomly initialising the atomic coordinates did not yield useful structures. However, relying on a reference could also induce larger biases.

1.3 Complexity and Implementation.

In light of all these options in the parametrization of the volume space, parametrizing the volume is in fact equivalent to defining a function $V(\tilde{V})$ from \mathbb{R}^3 to $\mathbb{R}(\mathbb{C})$. Based on Equation (1) (resp. Equation (2)), one can use V (resp. \tilde{V}) to generate a 2D image of resolution D , containing D^2 pixels. The complexity of simulating a projection depends on the parametrization of the volume, as summarized in Tables 2 and 3. Table 2 gives the memory cost of a representation along with the complexity of querying $V(x)$ (or $\tilde{V}(x)$) for $x \in \mathbb{R}^3$, depending on the volume parametrization. Table 3 shows the total complexity for computing a projection, depending on the volume parametrization and the representation space. One must first define a discrete

| Volume Param. | Space | Conformational Model | Approach | Hidden Variable | Known Variable | Reference Volume | |
|-------------------------|------------------|---|-----------------------------|-----------------|----------------|------------------|--|
| Discrete Representation | Voxel Grid | Image | CryoPoseNet ²³²³ | - | CTF | Free | |
| | | | | Rotation | - | | |
| | | Image | | - | Translation | | |
| | | | | - | CTF | | |
| | Fourier | Heterogeneous $z \rightarrow f(U(z_j), V_0)$ | 3DFlex ²¹²⁰ | Rotation | - | Free | |
| | | | | Translation | - | | |
| | | Homogeneous $z = (\mu_V, \sigma_V) \rightarrow V$ | | - | CTF | | |
| | | Heterogeneous $z \in \{1, \dots, K\} \rightarrow \{V_1, \dots, V_K\}$ | FSTdiff ²⁸²⁸ | Rotation | - | Yes | |
| | | Fourier | | Translation | - | | |
| | | | | - | CTF | | |
| | | RELION ¹⁸⁶ | Rotation | - | Free | | |
| | | | Translation | - | | | |
| Continuous Field | Neural Network | Image | CryoVAEGAN ³¹³¹ | CTF | - | Free | |
| | | Homogeneous $z = (\mu_V, \sigma_V, CTF_V) \rightarrow V_i(2D)$ | | 2D Rotation | - | | |
| | | Heterogeneous $z \rightarrow V_j$ | | - | Translation | | |
| | Gaussian Mixture | Fourier | CryoDRGN ¹⁴¹⁴ | - | CTF | | |
| | | Heterogeneous $z \rightarrow \{c_j, A_j, \sigma_j\}_{j \in [1, N]} \text{ or } \{\Delta c_j\}_{j \in [1, N]} ; (N \text{ floating})$ | | Rotation | - | Free | |
| | | Heterogeneous $z \rightarrow \{c_j\}_{j \in [1, N]} ; (N \text{ residues})$ | | Translation | - | | |
| | | Heterogeneous $z \rightarrow \{\Delta c_j\}_{j \in [1, N]} ; (N \text{ residues})$ | E2GMM ²²²² | - | CTF | Free or Yes | |
| | | Image | | - | Rotation | | |
| | | | | - | Translation | | |
| | | Image | CryoFold ²⁴²⁴ | - | CTF | | |
| | | | | - | Rotation | Free | |
| | | Image | atomVAE ¹⁰¹⁰ | - | Translation | | |
| | | | | Rotation | CTF | | |
| | | | | Translation | - | Yes | |

Table 1. Classification of reconstruction methods according to the parametrization nature of the volume V (or \tilde{V}), whether nuisance parameters are hidden or given, and whether the reconstruction is free from or anchored to a reference volume. The interpretation of the conformation variable z in terms of V or its parameters is also shown. When not specified, the latent variable z belongs to a vector space \mathbb{R}^L .

query grid \mathbf{G} of points in \mathbb{R}^3 (or \mathbb{R}^2 for a mixture of Gaussians). For a voxel grid and a neural network in Image space (resp. in Fourier space), \mathbf{G} is made of D^3 (resp. D^2) points $x \in \mathbb{R}^3$. In Image space, the rotation and the translation are applied to \mathbf{G} , the query grid is fed into V point-wise, the projection is done by summation along one axis of the grid, and we are finally left with a set of D^2 values corresponding to the D^2 pixels of the projection. In Fourier space, the translation can be applied after querying the volume \tilde{V}_j and we are directly left with the D^2 Fourier coefficients of the projection, based on the Fourier-slice theorem. Note that after applying the rotation and the translation, the points in the transformed query grid \mathbf{G}' do not necessarily have integer coordinates in $\Omega = \{1, \dots, D\}^3$. Therefore, with a voxel grid parametrization, one must also define an *interpolation kernel* to transform the function V (or \tilde{V}) defined on Ω into a function defined on \mathbb{R}^3 . Note that the use of an interpolation scheme necessarily induces artefacts in the generated image. The nature of these artefacts will both depend on the interpolation kernel and the representation space (image or Fourier). With a mixture of Gaussians, the rotation and the translation are applied to the centroids c_j and the projection can be analytically computed. The query grid is therefore made of D^2 points $x \in \mathbb{R}^2$ and is fed into the function $\int V(., z) dz : \mathbb{R}^2 \rightarrow \mathbb{R}$, which has a closed-form expression.

1.4 Defining the hidden variables and incorporating known variables

Because functions are complex objects, they are described through sets of real parameters in \mathbb{R}^p , where p is some integer value. In the case of cryo-EM, we denote as $\theta \in \mathbb{R}^p$ the parameters associated with the function V , that takes as input the conformation variable and domain coordinates. Thus, from a statistical viewpoint, the observed images X_i are generated through a function f_V of image-specific variables $H_i = (\text{PSF}_i, \sigma_i, t_i, R_i, z_i)$ and shared parameters θ :

$$X_i = f_V(H_i, \theta), \quad \text{for } i = 1, \dots, n, \quad (4)$$

where, given a description of the conformational landscape V , f_V is known and provided by Equations (1)-(2). The objective of this inference problem is thus to find the function V .

| Volume Param. | Voxel Grid | Continuous Field Neural Network | Mixture of Gaussians |
|----------------|------------------------------|---------------------------------------|----------------------|
| Notation | $\Omega = \{1, \dots, D\}^3$ | W weights width w depth d | N atoms |
| Memory | $O(D^3)$ | $O(W)$ | $O(N)$ |
| Query Cost Q | $O(1)$ | $O(dw^2)$ | $O(N)$ |

Table 2. Memory cost and computational complexity of querying $V(x)$ (or $\tilde{V}(x)$) for $x \in \mathbb{R}^3$, depending on the volume parametrization.

| Volume Param. | Voxel Grid or Neural Network | | Mixture of Gaussians |
|---------------------------------------|--|--|--|
| Space | Image | Fourier | Image |
| Query Grid | $\mathbf{G} \in \mathbb{R}^{3 \times D^3}$ | $\mathbf{G} \in \mathbb{R}^{3 \times D^2}$ | $\mathbf{G} \in \mathbb{R}^{2 \times D^2}$ |
| Rotation Translation Projection | $\mathbf{G}' = R^{-1}\mathbf{G} - \mathbf{t}$ $\sum V(\mathbf{G}')$ | $e^{i\mathbf{t} \cdot \mathbf{G}} \tilde{V}(R^{-1}\mathbf{G})$ | $\hat{c}_j = R c_j + \mathbf{t}$ $\int \hat{V}(\mathbf{G}, z) dz$ |
| Total Complexity | $O(QD^3)$ | $O(QD^2)$ | $O(ND^2)$ |

Table 3. Total complexity for simulating a projection, depending on the volume parametrization and the representation space. Q is given in Table 2.

This would be a standard statistical problem, were it not for the fact that the variables $H_i = (\text{PSF}_i, \sigma_i, t_i, R_i, z_i)$ (*i.e.* the covariates of the image) are unknown — also called "hidden" or "latent" in statistical terminology. Thus, they will have to be filled in — or "imputed". This yields a very difficult and expensive statistical problem: the number of unknowns and variables increases with the size n of the dataset, as for each particle image X_i , we need to (1) find the associated rotation R_i , translation t_i , PSF _{i} and conformation variable z_i to (2) impute a description of the conformational landscape V .

Specifying Hidden Variables The statistical problem above describes an extreme version of the cryo-EM reconstruction task where the model in Equation (4) is completely agnostic: all latent variables in $H_i = (\text{PSF}_i, \sigma_i, t_i, R_i, z_i)$ are assumed to be unknown and have to be imputed simultaneously during reconstruction. In reality, it is very difficult to recover all variables in H_i at once. Cryo-EM reconstruction methods vary according to the amount of information that is assumed known, *i.e.* which latent covariates in H_i are assumed to be given (which implies that they must be computed beforehand via an external algorithm), and which will need to be imputed during reconstruction. In fact, almost all the approaches presented in this review assume that the CTF (or PSF) has been estimated and is known; it is indeed possible to estimate the CTF independently from reconstructing the volume²⁹. The methods presented in this review subsequently differ in the latent variables that are effectively imputed: as shown in Table 1, some methods assume that the translation t_i is known and focus on the problem of estimating specific conformation variable z_i with associated $V(z_i)$, or vice versa. Section 2 will further explain Table 1 and present the inference methods that are used to impute the different latent variables in each approach.

Example: modeling Choices in RELION¹⁸ -Refine3D and RELION¹⁸ -Class3D. We illustrate the choices that can be made for inference, through the examples of RELION¹⁸ -Refine3D⁶ and RELION¹⁸ -Class3D¹⁹. RELION¹⁸ -Refine3D assumes the CTF to be known, and the volume $V^{(i)} = V$ to be a parameter. Given this image generative model, RELION¹⁸ -Refine3D uses a Bayesian approach that consists of (a) modeling the unknown parameter V as a random variable, *i.e.* modeling the Fourier coefficients of the volume \tilde{V}_j as random variables, (b) modeling latent variables in H_i as random variables, *i.e.* assuming that the Fourier poses (describing particles' orientation and position) are random variables, and (c) specifying probability distributions on these random variables, *i.e.* priors in statistical terminology. Specifically, RELION¹⁸ -Refine3D assumes that the Fourier coefficients \tilde{V}_j are sampled from independent Gaussian distributions: $\tilde{V}_j \sim N(0, \tau_j^2)$, while the pose latent variables are assumed to be uniformly distributed. The purpose of the inference is to find the parameters of the probability distributions — *i.e.* for the Gaussian variables \tilde{V}_j , the means and standard deviations — that best explain the observed data. RELION¹⁸ -Class3D operates similarly, but each image is generated from a set of K volumes, V_1, \dots, V_K , which are parameters modeled as random variables.

2 Inference

Section 1 introduced the generative model for cryo-EM images, its possible parametrizations — with an emphasis on the parametrizations of the biomolecular volume —, and corresponding objective functions. This Section details the inference methods that are then used to find an optimal solution for the function V of Equation (4), while accounting for the unknown hidden variables H_i . Whether V is defined on a discretized 3D grid or continuous 3D domain, we refer to the parameters associated with this function as θ .

Setting Up the Inference Problem: Observed Likelihood vs Full Likelihood Once the latent variables are specified, one can properly formalize the inference problem and specify the appropriate objective function — whose optimization allows to recover θ . A generative model of the form in Equation (4) provides a probability distribution of each image $p_\theta(x) = p(x|\theta)$. Given n observed images x_1, \dots, x_n , the goal of inference is to estimate the model's parameters θ that maximize the observed

log-likelihood $L(X, \theta)$:

$$L(X, \theta) = \log p_{\theta}(x_1, \dots, x_n) = \sum_{i=1}^n \log p_{\theta}(x_i) = \sum_{i=1}^n \log \int_{h_i} p_{\theta}(x_i, h_i) dh_i \quad (5)$$

These maximum-likelihood (ML) approaches view the parameter θ as an unknown real value (as opposed to a random variable). In cryo-EM, the generative model in Equation (4) depends on hidden variables H_i , and it would be simpler to compute the full likelihood of each observation $p(x_i, h_i, \theta)$, if only the h_i were observed. By contrast, the “observed likelihood” $p_{\theta}(x_i)$ is a marginal likelihood that requires an integral over the h_i . This is difficult to compute directly, or statistically “intractable”.

Adding Priors: From Maximum Likelihood (ML) to Maximum a Posteriori (MAP) Alternatively, the parameter θ can be viewed as a random variable with a prior $p(\theta)$. In this case, inference seeks to estimate θ through the maximum of its posterior distribution $p(\theta|x_1, \dots, x_n)$, written in its logarithm form as:

$$\log p(\theta|x_1, \dots, x_n) \propto \log p(\theta, x_1, \dots, x_n) = \log p_{\theta}(x_1, \dots, x_n) + \log p(\theta) = L(X, \theta) + \log p(\theta). \quad (6)$$

This typically increases robustness by embedding in the design of the algorithm the inherent variability and uncertainty associated with these variables. In fact, following Scheres⁶, this can be viewed as a kind of regularization. The Maximum a Posteriori (MAP) approaches are chosen in Relion-Refine3D and Relion-Class3D¹⁸, FSTdiff²⁸, and CryoSPARC⁹.

We observe that the ML and MAP objectives in Equations (5)-(6) only differ through the prior term $\log p(\theta)$, while the challenge of the optimization stems from the intractable term $L(X, \theta)$. Both approaches traditionally employ the same optimization techniques. In what follows, we thus describe these techniques by focusing solely on the term $L(X, \theta)$. We begin by highlighting the common statistical thread central to the optimization methods used in the literature, before diving into the specifics and differences between techniques.

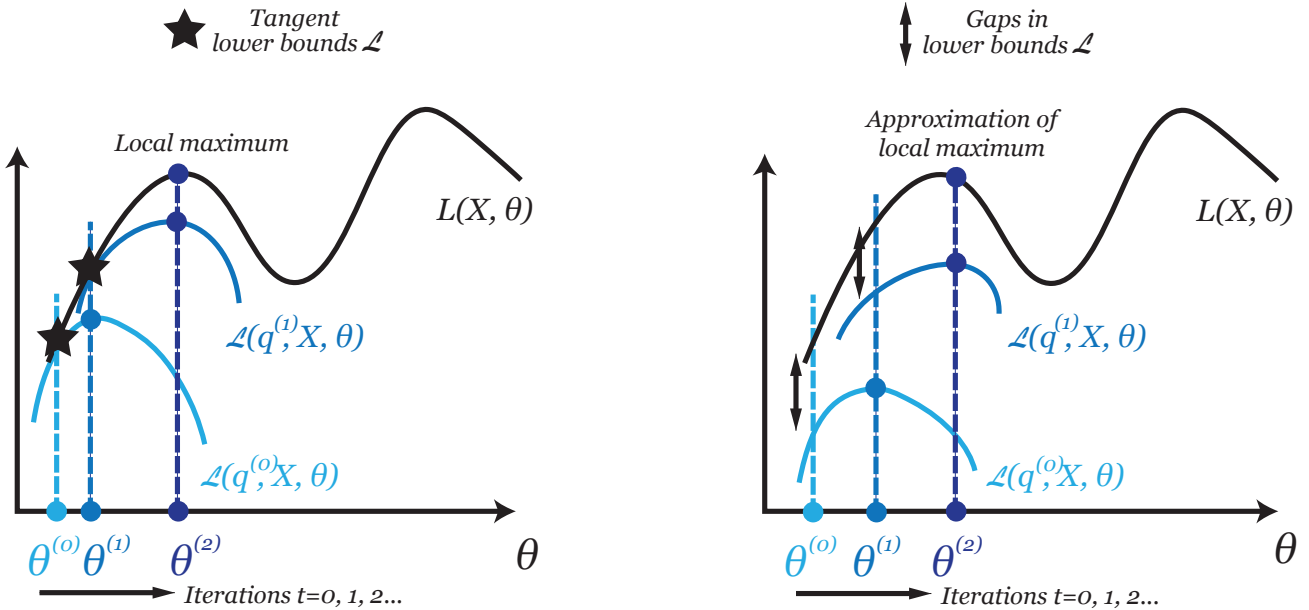


Figure 3. Maximization of the log-likelihood $\theta \rightarrow L(X, \theta)$ in θ by maximizations of a series of lower bounds: $\mathcal{L}(q^{(0)}, X, \theta)$, $\mathcal{L}(q^{(1)}, X, \theta)$, etc. The $\theta^{(t)}$'s across iterations $t = 0, 1, 2, \dots$ are represented by colored dots and correspond to successive maxima of the lower bounds. Left: The lower bounds are tangent to $\theta \rightarrow L(X, \theta)$, which is realized when q is the posterior of the hidden variables. Right: The lower bounds are not tangent to $\theta \rightarrow L(X, \theta)$, but show a “gap” that corresponds to the KL divergence between q and the posterior of the hidden variables, see Equation (7).

Evidence Lower Bound (ELBO) The cryo-EM reconstruction inference methods typically maximize the log-likelihood through the maximization of some Evidence Lower Bound (ELBO). We have established above that the term $L(X, \theta)$ in the objectives of Equations (5)-(6) is intractable. The full likelihood $L(X, H, \theta)$ would be easier to optimize with respect to θ , as its definition does not involve an integral, but it depends on hidden variables H which are inaccessible. Thus, to maximize $L(X, \theta)$ over θ , the trick consists in proposing a distribution q for the hidden variables H , and maximizing a series of tractable, “easily” computable lower-bounds $\mathcal{L}(q, X, \theta)$ for $L(X, \theta)$ in an iterative fashion — see Figure 3. By iteratively maximizing these lower bounds with respect to θ , the true likelihood $L(X, \theta)$ also increases. The hope is that the value of θ obtained through their maximization will be close to the value realizing the maximum of $L(X, \theta)$, if the lower bounds are tight enough — *i.e.* small

“gaps” in Figure 3.

The lower bounds $\mathcal{L}(q, X, \theta)$ are found by showing that, for any probability distribution q_i on the variables h_i , the observed log-likelihood can be written as the sum of two terms (derivations provided in Appendix 4):

$$L(X, \theta) = \mathcal{L}(q, X, \theta) + \sum_{i=1}^n \text{KL}(q_i(h_i) \parallel p_\theta(h_i|x_i)) = \sum_{i=1}^n \left[\mathcal{L}_i(q_i, x_i, \theta) + \text{KL}(q_i(h_i) \parallel p_\theta(h_i|x_i)) \right] \quad (7)$$

where KL is the **Kullback-Leibler divergence (KL)** defined as $\text{KL}(q \parallel p) = \int_h q(h) \log q(h) dh - \int_h q(h) \log p(h) dh$, and the terms \mathcal{L}_i write:

$$\mathcal{L}_i(q_i, x_i, \theta) = \int_{h_i} q_i(h_i) \log p_\theta(x_i|h_i) dh_i - \text{KL}(q_i(h_i) \parallel p_\theta(h_i|x_i)). \quad (8)$$

The divergence $\text{KL}(q(h_i) \parallel p_\theta(h_i|x_i))$ in Equation (7) is always non-negative. Thus, for any distribution q in any family of distribution \mathcal{Q} , the function $\theta \rightarrow \mathcal{L}(q, X, \theta)$ indeed provides a valid lower-bound to $\theta \rightarrow L(X, \theta)$, called the Evidence Lower Bound (ELBO):

$$\forall q \in \mathcal{Q}, \forall \theta, \quad \mathcal{L}(q, X, \theta) \leq L(X, \theta).$$

Refining the distributions $q_i^{(t)}$ at each iteration t until convergence of the $\theta^{(t)}$ provides a series of computable lower bounds to the log-likelihood that, in turn, allows to estimate θ .

Inference Methods Based on an ELBO. Inference methods in Cryo-EM subsequently differ in the way they compute the lower bounds $\mathcal{L}(q, X, \theta)$, i.e. in the choices of the distributions $q_i^{(t)}$ at each iteration t .

- Computing the posteriors $p_\theta(h_i|x_i)$ using the current estimated value $\theta^{(t)}$ of θ allows choosing $q_i(z^{(t)}) = p_{\theta^{(t)}}(h_i|x_i)$ for each i at iteration t — see the green probability distribution in Figure 4. In this case, the inequality:

$$\mathcal{L}_i(p_{\theta^{(t)}}(h_i|x_i), X, \theta) \leq L_i(X, \theta),$$

becomes an equality for $\theta^{(t)} = \theta$. This makes the lower-bound $\mathcal{L}(q, X, \theta)$ tangent to $L(X, \theta)$ at $\theta = \theta^{(t)}$: progressively maximizing $\mathcal{L}(q, X, \theta)$ with respect to θ will induce convergence to a local maximum of $L(\theta)$, as seen in Figure 3 (left). This is the focus of the **Expectation-Maximization (EM)** algorithm described in Subsection 2.1 and first column of Table 4.

- For computational reasons, we can choose to have $q_i(z^{(t)})$ approximate the posteriors $p_{\theta^{(t)}}(h_i|x_i)$ by:
 - (i) their “mode”, i.e. the value \hat{h}_i of h_i that maximizes them: q_i effectively becomes a Dirac distribution at \hat{h}_i , represented in gray in Figure 4,
 - (ii) or a general distribution q_i within a family \mathcal{Q} : q is for example a Gaussian distribution, such as the one represented in brown in Figure 4.

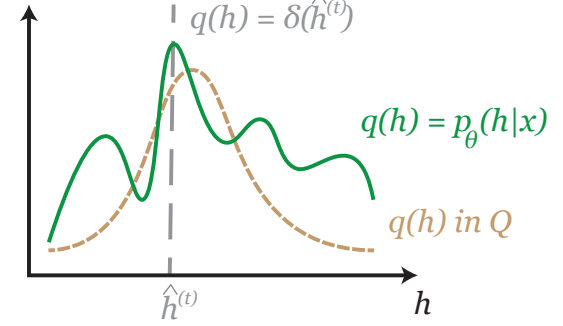


Figure 4. Possible choices for the distribution q chosen on the hidden variables h , where we have dropped the indices i for convenience of notations. The choice of q determines the lower bounds to $L(X, \theta)$ in Figure 3. The inference methods used in cryoEM reconstruction can be contrasted by the choice of q : as the true posterior $p_\theta(h|x)$ represented by the green line, as the Dirac distribution $\delta(h)$ represented by the vertical dashed gray line or as a distribution within a known parameterized family \mathcal{Q} , such as the family of Gaussian distributions, represented by the brown dashed line.

Then, the gap between $L(X, \theta)$ and the ELBO $\mathcal{L}(q, X, \theta)$ is $\text{KL}(q_i(h_i) \parallel p_\theta(h_i|x_i))$ and is a function of q_i which we wish to minimize — see Figure 3 (right). The challenge of these methods is then to find the “best proxies” q_i for the unknown posteriors $p_{\theta^{(t)}}(h_i|x_i)$ that make the KL term small and allow us to best optimize the parameters θ . Approximations (i) and (ii) are the focus of Subsections 2.2 and 2.3 respectively, and the last two columns of Table 4.

2.1 Expectation-maximization (EM) Algorithm

Historically, inference in latent variable models has been achieved through the Expectation-maximization (EM) algorithm³⁰. The EM algorithm is often introduced as a data imputation technique (described in Appendix 4) but it can also be understood as a dual ascent algorithm — a perspective that allows unifying the cryoEM inference methods and that we present here.

EM as a Dual Ascent Algorithm The EM algorithm can be seen as a dual ascent procedure, *i.e.* as a maximization-maximization procedure, that leverages Equation (7) rewritten as: $\mathcal{L}(q, X, \theta) = L(X, \theta) - \sum_{i=1}^n \text{KL}(q_i(h_i) \parallel p_\theta(h_i|x_i))$. Starting with an initial guess $\theta^{(0)}$ of the parameter, the EM algorithm performs two steps at each iteration t :

(a) Inference on hidden variables (E-step) Given the current $\theta^{(t-1)}$, maximize each $\mathcal{L}_i(q, \theta^{(t-1)})$ with respect to the distribution q defined on the hidden variables h_i :

$$\text{For each } i = 1, \dots, n: \quad q_i^{(t)}(h_i) = \arg \max_q \mathcal{L}_i(q, X, \theta^{(t-1)}) = p_{\theta^{(t-1)}}(h_i | x_i). \quad (9)$$

This choice $q_i^{(t)}(h_i) = p_{\theta^{(t-1)}}(h_i | x_i)$ corresponds to the green distribution in Figure 4 and makes the lower bound \mathcal{L} tangent to L at $\theta^{(t-1)}$ in Figure 3 (left).

(b) Maximization on the model's parameters (M-step) Given the current $q^{(t)} = \{q_1^{(t)}, \dots, q_n^{(t)}\}$, maximize $\mathcal{L}(q^{(t)}, X, \theta)$ with respect to the model's parameter θ :

$$\theta^{(t)} = \arg \max_{\theta} \mathcal{L}(q^{(t)}, X, \theta) = \arg \max_{\theta} \sum_{i=1}^n \mathcal{L}_i(q_i^{(t)}, X, \theta). \quad (10)$$

The argument maximum of \mathcal{L} is used to updated $\theta^{(t-1)}$ to $\theta^{(t)}$ in Figure 3 (left).

These steps are iterated until convergence in θ . In this view, one first finds the "best" lower bound to $L(X, \theta)$ given $\theta^{(t)}$, by choosing the one that is tangent to $L(X, \theta)$ at $\theta^{(t)}$, and subsequently maximizes this bound. We highlight that only one gradient step on the respective objective functions $\mathcal{L}(q, X, \theta^{(t-1)})$ and $\mathcal{L}(q^{(t)}, X, \theta)$ could be performed in the respective E-step or M-step. This gives rise to "gradient EM" methods, which we will refer to later, as all methods introduced in the next Subsections can be formulated as "gradient" methods too.

Computational Bottleneck: E-step. We note that the result of the maximization in the E-step is known: it is the posterior of the latent variable h_i given x_i and with current estimate $\theta^{(t-1)}$:

$$p_{\theta^{(t-1)}}(h_i | x_i) = \frac{p_{\theta^{(t-1)}}(x_i | h_i) p(h_i)}{p_{\theta^{(t-1)}}(x_i)} = \frac{p_{\theta^{(t-1)}}(x_i | h_i) p(h_i)}{\int_{h_i} p_{\theta^{(t-1)}}(x_i, h_i) dh_i}. \quad (11)$$

Thus, the maximization in this step boils down to computing $p_{\theta^{(t-1)}}(h_i | x_i)$ for each $i = 1, \dots, n$. The integral in Equation (11) represents the main computational bottleneck in cryo-EM reconstruction methods.

EM in RELION¹⁸ and CryoSPARC⁹ The computation of the posterior could be achieved by using a closed form for the expression of the probability $p(h_i | x_i, \theta^{(t-1)})$ and maximizing over its parameters. In cryo-EM generative models, however, such a closed form is not known. Alternatively, one can evaluate $p_{\theta^{(t-1)}}(h_i | x_i)$ for each h_i discretized on a grid by computing the integral in Equation (11) via a Riemann sum as in RELION¹⁸ or via Importance Sampling as in CryoSPARC⁹. RELION¹⁸ and CryoSPARC⁹ use the EM algorithm with MAP estimation of θ , as opposed to ML estimation. Additionally, CryoSPARC⁹ uses stochastic gradient descent for the maximizations in the M-step, at each iteration t .

The E-step of the EM algorithm still represents a major bottleneck, despite many advances leveraging GPU computing. Alternative approaches thus focus on avoiding the evaluation of the posterior and specifically the computation of its integral in Equation (11).

2.2 Modal EM algorithm

The computational bottleneck observed in the EM algorithm has also motivated the use of approximations in the E-step. The modal approximation of EM amounts to finding a proxy for the posterior $p_{\theta^{(t-1)}}(h_i | x_i)$ in the E-step. This approximation replaces the posterior by its "mode" $\hat{h}_i = \arg \max_h p_{\theta^{(t-1)}}(h | x_i)$, i.e. the most probable \hat{h}_i for each image x_i .

Modal EM as a Dual Ascent Algorithm The E-step of the EM algorithm is replaced by its modal approximation, but the M-step is largely unchanged:

(a) Inference on hidden variables h_i Given current $\theta^{(t)}$, compute the modes:

$$\text{For each } i = 1, \dots, n: \quad \hat{h}_i^{(t)} = \arg \max_h p_{\theta^{(t-1)}}(h | x_i) = \arg \max_h p_{\theta^{(t-1)}}(x_i | h) p(h). \quad (12)$$

This amounts to choosing $q_i^{(t)}(h_i) = \delta(\hat{h}_i^{(t)})$, the Dirac distribution at $\hat{h}_i^{(t)}$, represented in gray in Figure 4. This choice for $q_i^{(t)}(h_i)$ creates a lower bound \mathcal{L} that may not be tangent to L in Figure 3 (right).

(b) Maximization on model's parameter θ The parameter θ is updated via:

$$\theta^{(t)} = \arg \max_{\theta} \sum_{i=1}^n \mathcal{L}(\delta(\hat{h}_i^{(t)}), \theta) = \arg \max_{\theta} \sum_{i=1}^n p_{\theta}(x_i, \hat{h}_i^{(t)}). \quad (13)$$

The argument maximum of \mathcal{L} is used to updated $\theta^{(t-1)}$ to $\theta^{(t)}$ in Figure 3 (right), just as in the EM algorithm in Figure 3 (left).

We note that the computation of the modes in Step (a) do not require the evaluation of the integral defining the posteriors $p_{\theta^{(t-1)}}(h|x_i)$ in Equation (11), as this integral does not depend on h .

Modal EM in RELION¹⁸, CryoSPARC⁹, 3DFlex²¹, CryoDRGN¹⁴, CryoFold²⁴ The EM algorithm with modal approximation is used in cryo-EM in CryoSPARC⁹, 3DFlex²¹, CryoDRGN¹⁴ and CryoFold²⁴ to infer the latent variable associated with the rotation R_i . In other words, they estimate the best rotation \hat{R}_i for each input image i , relying on a branch-and-bound optimization algorithm to address this maximization. This approach is also used in RELION¹⁸ to estimate the best noise variance $\hat{\sigma}_i$ that is associated with each image i .

2.3 Variational EM algorithm

The modal approximation in the EM algorithm speeds up the E-step; yet it has the drawback of summarizing the whole posterior distribution $p_{\theta^{(t)}}(h|x_i)$ by a single estimate \hat{h}_i , reducing accuracy and leading to non-tangent lower bounds \mathcal{L} . **Variational Inference (VI)**, also known as Variational Bayes, has appeared in cryo-EM as a compromise between EM and modal EM during the computation of the E-step.

VI replaces the evaluation of the posterior of the latent variables $p_{\theta^{(t-1)}}(h|x_i)$, by an optimization converging to an approximation q of this posterior distribution. VI selects q from some parametric family of distributions \mathcal{Q} , called the “variational family”, such that q is the “closest” to the posterior, where “closest” is defined in terms of the KL divergence (see Equation (14) below).

The variational family $\mathcal{Q} = \{q_\eta|\eta\}$ with parameters η is typically chosen to be a family of Gaussian distributions, in which case η represents the mean and variance, i.e. $\mathcal{Q} = \{q_\eta = N(\mu, \sigma)|\eta = (\mu, \sigma)\}$. Other approaches consider the variational family of Gaussian distributions with fixed isotropic variance σ_0 , i.e. $\mathcal{Q} = \{q_\eta = \mathcal{N}(\eta, \sigma_0)|\eta\}$. In modal EM, the parametric family can be seen as a family of Dirac distributions, as in Equation (13).

Variational EM as a Dual Ascent Algorithm The E-step of the EM algorithm is replaced by VI and the M-step is unchanged. The VI framework thus gives rise to a variational EM which performs the following two steps at each iteration (t):

(a) Inference on hidden variables h_i The n parameters η_i corresponding to each q_i are computed via:

$$\text{For each } i = 1, \dots, n: \quad \eta_i^{(t)} = \arg \min_{\eta} KL(q_\eta || p_{\theta^{(t-1)}}(h_i|x_i)) \quad (14)$$

This choice for q is represented in brown in Figure 4. Similarly to the Modal EM, this creates a lower bound \mathcal{L} that may not be tangent to L in Figure 3 (right).

(b) Maximization on model's parameter θ The parameter θ is updated via:

$$\theta^{(t)} = \arg \max_{\theta} \sum_{i=1}^n \mathcal{L}_i(q_{\eta_i}^{(t)}, \theta). \quad (15)$$

The argument maximum of \mathcal{L} is used to update $\theta^{(t-1)}$ to $\theta^{(t)}$ in Figure 3 (right), just as in the EM and the Modal EM algorithms.

Thus, VI in the E-step replaces the samplings in evaluation of the true posterior by an optimization on the fewer parameters η_i parametrizing each approximate posterior q_{η_i} , which can be efficiently conducted with (stochastic) gradient descent. In this sense, it also represents a solution to the computational bottleneck of the E-step.

Variational EM in 3DFlex²¹ and FSTdiff²⁸ Variational gradient EM is used in 3DFlex²¹ to infer the rotation variable R_i , using the variational family of Gaussian distributions with fixed isotropic variance σ_0 . Variational EM is also used in FSTdiff²⁸ in the context of homogeneous reconstruction. Here, VI happens both in Step (a), to estimate the approximate posterior of the rotation R_i , and in Step (b) to also estimate the approximate posterior of the volume V , which is a parameter included in θ . The approximate posterior of V provides an approximate measure of uncertainty on the homogeneous reconstruction.

2.4 Introducing Amortized Inference

The previous methods have the drawback of learning one (approximate) posterior for each hidden variable in $h_i = (R_i, t_i, \text{PSF}_i, z_i)$, and for each image i in $1, \dots, n$. This is computationally expensive, as the number of values to estimate increases very rapidly as n , the number of images, increases. As a result, recent methods rely on **Amortized Inference (AI)** for the E-step, either within the modal EM of Subsection 2.2, or within the variational EM of Subsection 2.3.

Amortized inference (AI) collapses the n optimizations problems of the E-step into one. Instead of solving an optimization problem for each i and finding \hat{h}_i (in modal EM) or η_i defining q_{η_i} (in variational EM), AI optimizes the parameters ξ of a function Enc_ξ that predicts \hat{h}_i or η_i when given x_i as input, i.e.: $\text{Enc}_\xi(x_i) \simeq \hat{h}_i$ or $\text{Enc}_\xi(x_i) \simeq \eta_i$. The function Enc is traditionally called an encoder. Inference is made more tractable, but adds an additional error, called the amortization error.

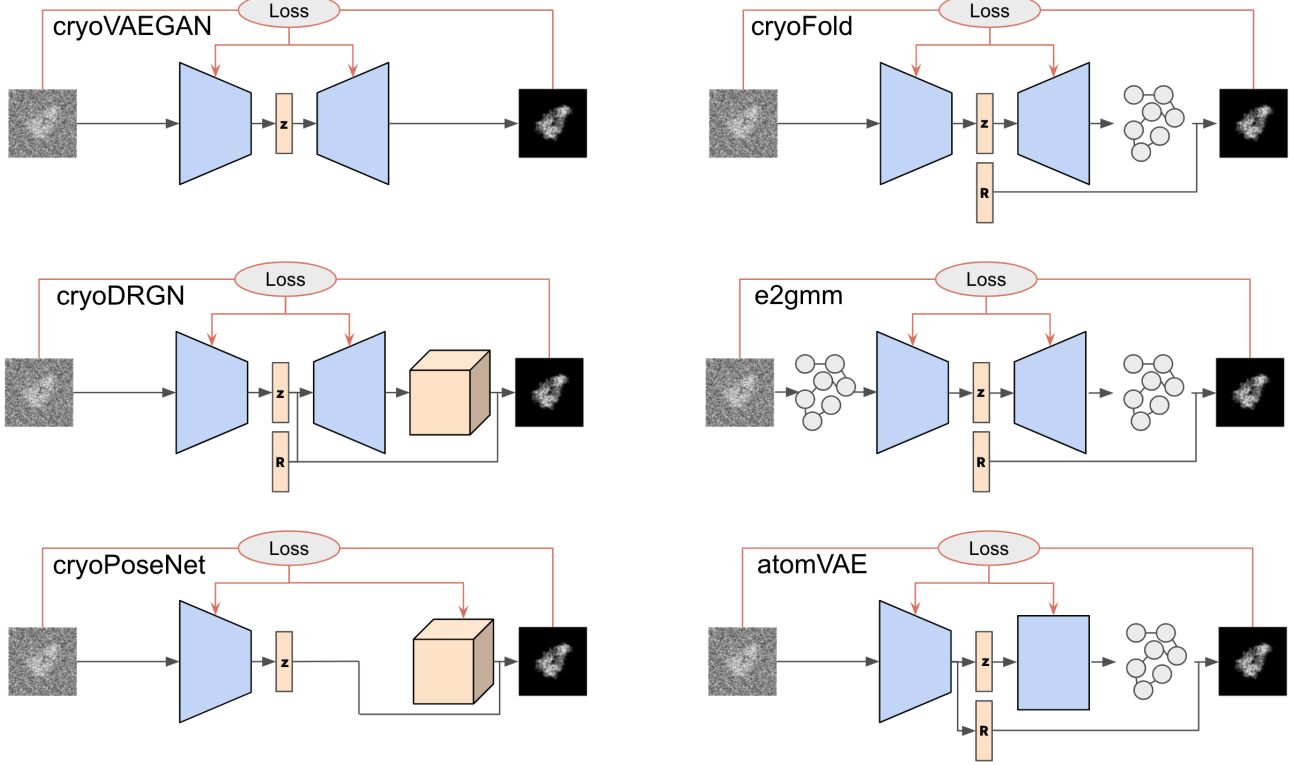


Figure 5. Comparison fo the different autoencoder architectures.

Amortized Variational EM as Dual Optimization Algorithm AI in the E-step of variational EM leads to an amortized variational EM:

(a) Inference on hidden variables h_i The parameters ξ parametrizing the encoder is computed via:

$$\xi^{(t)} = \arg \max_{\xi} \sum_{i=1}^n KL(q_{\text{Enc}_{\xi}(x_i)} || p_{\theta^{(t-1)}}(h_i | x_i)) \quad (16)$$

which generates n distributions $q_{\eta_i}^{(t)}$ parametrized by $\eta_i = \text{Enc}_{\xi^{(t)}}(x_i)$.

(b) Maximization on model's parameter θ The parameter θ is updated via:

$$\theta^{(t)} = \arg \max_{\theta} \mathcal{L}(q_{\eta_i}^{(t)}, \theta). \quad (17)$$

For EM and variational EM algorithms, the optimizations (a)-(b) can be conducted fully at each iteration, or only a gradient step can be performed — see “gradient EM” in Subsection 2.1. We call these methods amortized variational EM and amortized variational gradient EM respectively. The main realizations of amortized variational gradient EM in cryo-EM come through (variational) autoencoders, which we describe next.

(Variational) Autoencoders as Deep Learning Architectures (Variational) autoencoders are known as deep learning neural networks consisting of an encoder and a decoder. The encoder takes an image X_i as input, outputs a latent variable h_i . The decoder inputs the latent variable h_i and outputs a reconstruction \hat{X}_i of the original image X_i . Note that, even though we use the term “reconstruction” here, this only refers to the reconstruction of the original 2D image, and not of the molecular volume.

(a) Encoder - Inference on hidden variables h_i The purpose of the encoder is to output the latent variables h_i that are presented as a low-dimensional (compressed) representation of the information encoded in the image X_i . The function Enc_{ξ} is practically implemented through a neural network with weights ξ , such that: $h_i = \text{Enc}_{\xi}(h_i)$.

(b) Decoder - Estimation of model's parameter θ The purpose of the decoder is to input the latent h_i and output the reconstructed image \hat{X}_i . The decoder is therefore a function Dec_{θ} such that: $\hat{X}_i = \text{Dec}_{\theta}(h_i)$, that is traditionally implemented as a neural network with weights θ . As such, the decoder is an instance of a generative model described in Section 1. In

cryo-EM, the architecture of the decoder can be guided by the image formation model in Equations (1)-(2), and therefore consists of a tailored architecture that goes beyond the conventional fully connected networks or convolutional neural networks.

The parameters ξ and θ of the encoder and the decoder are typically estimated through stochastic gradient descent via backpropagation through the neural network. The loss function that is minimized gives rise to two optimizations for (a) the encoder and (b) the decoder, which can be interpreted as extensions of the E-step and the M-step of the EM algorithm.

We note that (variational) autoencoders perform minimizations, as opposed to maximizations, since deep learning methods traditionally minimize a loss function that represents an equivalent of the negative log-likelihood or the negative ELBO. We detail the optimization procedures of the auto-encoder and variational autoencoder in the supplementary materials.

AE and VAE in CryoDRGN¹⁴, CryoFold²⁴, CryoVAEGAN³¹, CryoPoseNet²³, E2GMM²², atomVAE¹⁰ Amortized variational (gradient) EMs are the most common type of unsupervised deep learning approaches implemented for cryo-EM reconstruction.

CryoPoseNet²³ and E2GMM²² use an autoencoder, and E2GMM²² additionally implements an variational autoencoder with a variational family of Gaussian distributions with fixed isotropic variance σ_0 . The AE architecture is used in CryoPoseNet²³ with a traditional L2 reconstruction loss and in E2GMM²² with a tailored reconstruction loss that relies on the Fourier ring correlation (FRC) reconstruction metric.

CryoVAEGAN³¹, CryoDRGN¹⁴, CryoFold²⁴, and atomVAE¹⁰ use VAEs with a variational family of Gaussian distributions with diagonal covariance matrix. CryoVAEGAN³¹ uses this inference method to infer the rotation R_i and the CTF $_i$ latent variables. CryoDRGN¹⁴ and CryoFold²⁴ use this method to infer the conformation variable z_i . atomVAE¹⁰ uses it to infer the rotation R_i and the conformation variable z_i .

The VAE architecture is used in CryoDRGN¹⁴ with the negative ELBO loss, and in CryoVAEGAN³¹ with the negative ELBO loss extended with the β hyper-parameter described in the supplementary materials, an additional geometric regularization term, and the reconstruction loss relies on the binary cross-entropy as opposed to the L2 reconstruction loss. atomVAE¹⁰ also implements a VAE, with a modified ELBO loss that relies on important sampling (not detailed in this review), that leverages the β hyperparameter and additionally includes a “structure loss” — see supplementary materials.

We observe that most methods actually do not strictly follow the original optimization method of the VAE, but supplement it with a wide range of additional losses or modifications. These testify to the difficulties encountered in training these algorithms.

2.5 Generative Adversarial Networks

Cryo-EM reconstruction methods from Subsections 2.2-2.3 have naturally explored adaptations of the computationally expensive E-step from the EM algorithm of Subsection 2.1. As a result, they differ in their inference on the hidden variables of the generative model. Yet, the only hidden variable of interest is the conformation variable and associated molecular volumes. As a result, recent works have explored methods that avoid the inference on the “nuisance” latent variables altogether. This is the approach taken by [Generative Adversarial Network \(GAN\)](#).

Generative Adversarial Networks as Minimax Games A generative adversarial model (GAN)³² is a method that estimates the parameters of a generative model, such as the one in Equation (4), through an adversarial process. The GAN trains a “generator” to produce images x_i that best capture the training data distribution, while a discriminator estimates the probability that a given image x_i came from the training data rather than the generator.

In other words, the generator and discriminator play the following two-player minimax game with value function V :

$$V = \min_{\theta} \max_{\phi} \mathbb{E}_{x \sim p_{\text{data}}(x)} [\log \text{Dis}_{\phi}(x)] + \mathbb{E}_{h \sim p(h)} [\log (1 - \text{Dis}_{\phi}(f_{V_{\theta}}(h)))] ,$$

where the generator is the cryo-EM generative model defined via the function $f_{V_{\theta}}$ in Equation (4) and the discriminator has weights ϕ and is denoted by Dis_{ϕ} . In this equation, $p_{\text{data}}(x)$ represents the probability distribution of the images, and $p(h)$ is a prior distribution on the hidden variables. The GAN training iterates two steps:

(a) Discriminator - Update of parameters ϕ , according to the gradient step:

$$\phi^{(t+1)} = \phi^{(t)} + \nabla_{\phi} \frac{1}{n} \sum_{i=1}^n \left[\log \text{Dis}_{\phi}(x_i) + \log \left(1 - \text{Dis}_{\phi}(f_{V_{\theta}^{(t)}}(h_i)) \right) \right] , \quad (18)$$

(b) Generator - Estimation of model’s parameter θ , according to the gradient step:

$$\theta^{(t+1)} = \theta^{(t)} - \nabla_{\theta} \frac{1}{n} \sum_{i=1}^n \left[\log \left(1 - \text{Dis}_{\phi^{(t)}}(f_{V_{\theta}}(h_i)) \right) \right] , \quad (19)$$

where in each Step (a) or (b), the “hidden variables” h_i are sampled according to a prior distribution p_h . Even though a GAN iterates two steps, including one step related to the estimation of the model’s parameters, its framework differ from the variations

| | Posterior $p(h_i x_i)$ | Mode \hat{h}_i | | Variational $q(h_i)$ | |
|--------------------------------|---|---|--|--|--|
| | | Non-Amortized | Amortized (encoder) | Non-Amortized | Amortized (encoder) |
| Distribution on h_i | $p(h_i x_i)$ | $\arg \max_{h_i} p(h_i x_i)$ | $\text{Enc}_\xi(x_i)$ | $q_{\eta_i} \in \mathcal{Q}$ | $q_{\text{Enc}_\xi(x_i)} \in \mathcal{Q}$ |
| Name | EM | Approx. EM | Am. EM / AE | Var. EM / AD | Var. Am. EM / VAE |
| Inference on h_i (E-step) | RELION ¹⁸ (rotation R_i and conformation z_i) (*) | RELION ¹⁸ (noise σ_i) (*) | CryoPoseNet ²³ (rotation R_i) | FSTdiff ²⁸ (rotation R_i and conformation V) | CryoDRGN ¹⁴ (conformation z_i) |
| | | CryoSPARC ⁹ (rotation R_i) (*) | E2GMM ²² (conformation z_i) | 3DFlex ²¹ (conformation z_i) | CryoVAEGAN ³¹ (2D rotation R_i and CTF_i) |
| | | CryoDRGN ¹⁴ (rotation R_i) (*) | | | atomVAE ¹⁰ (rotation R_i and conformation z_i) |
| | | CryoFold ²⁴ (rotation R_i) (*) | | | CryoFold ²⁴ (conformation z_i) |
| | | 3DFlex ²¹ (conformation z_i) | | | |

Table 4. Classification of cryoEM reconstruction algorithms with respect to the inference on the hidden variables h_i . The inference step updates the posterior $p(h_i|x_i)$, or its mode \hat{h}_i , or a variational approximation $q(h_i)$ of it — which corresponds to the 3 main columns of the table. The works by Zhong et al. (2019, 2021) are classified in several cells, as inference of the conformation z_i is performed via a VAE, but the inference of the poses R_i is performed with an optimization algorithm. The notation (*) specifies that the optimization associated with this step is fully performed (until convergence to local extremum) while its absence indicates that only a gradient step is taken toward the optimum.

of the EM algorithm in the sense that the hidden variables are not inferred: it is enough to be able to randomly sample from them from some prior distribution.

GANs in CryoGAN²⁷ and Multi-CryoGAN³³ CryoGAN²⁷ uses a GAN to perform homogeneous reconstruction of molecular volumes, while using uniform sampling on the rotation, translation and CTF hidden variables. Multi-CryoGAN³³ introduces heterogeneous reconstruction with this approach. Both CryoGAN²⁷ and Multi-CryoGAN³³ use the Wasserstein variant of the traditional GANs.

2.6 Summary of Inference Methods

Table 4 summarizes the inference methods and classifies the different algorithms by the type of inference chosen for each of variable within $h_i = (R_i, t_i, \text{PSF}_i, z_i)$. We remark that some methods mix and match, using for example a variational EM for the hidden rotation variable R_i and a VAE for the conformation variable z_i . Researchers effectively choose which parameters or latent variables are assumed to be known, which will be estimated, and if so with which inference methods. The GANs are not included in the Table.

We also note that, due to the volume of the data in cryo-EM, exact Bayesian inference procedures — such as Gibbs sampling³⁴ or Hamiltonian Monte Carlo³⁵ — cannot be deployed because of computational constraints. Cryo-EM reconstruction methods thus have to use the scalable inference schemes described in this review, that possibly approximate in the sense that they often approximate the true posterior of the hidden variables by another distribution q .

3 Discussion

Given the wide number of options to reconstruct molecular volumes from cryo-EM images described throughout this review — both in terms of the parametrization of the problem, as well as in the choice of the inference method —, a natural question concerns the relative advantages of each method against the others: *which of these methods is in fact the best approach?*

The quantitative assessment of the performance of these reconstruction methods usually comprises two main axes: (a) an evaluation of the method’s ability to provide good **spatial resolution** (i.e., we want to distinguish the different atoms) and (b) an evaluation of its ability to distinguish different conformations (i.e. **conformation resolution**).

Assessing Spatial Resolution: Toolbox Evaluation of the quality of a spatial reconstruction is typically done through a set of experiments on synthetic and experimental data. Synthetic data is usually simulated with a known reference volume that is projected using a forward model such as the one in Eq. 1 to generate “mock images” with known CTF, rotation angles and

controlled signal-to-noise ratios. Synthetic datasets allow in particular to evaluate a method’s accuracy in recovering any hidden variables, while keeping the others fixed and assuming that they are known. The metrics used to evaluate the quality of the reconstruction in synthetic and experimental settings typically involve computing ¹:

Fourier Shell Correlation (FSC) between two maps U and V : As described in greater details by Singer et al⁷, this quantity measures the correlation over a 3D shell between two reconstructed volumes, defined as:

$$FSC(k) = \frac{\sum_{s \in S_k} U_s V_s^*}{\sqrt{\sum_{s \in S_k} |U_s|^2 \sum_{s \in S_k} |V_s|^2}}$$

where S_k is the set of Fourier voxels in a spherical shell at distance k from the origin, and U and V are the Fourier transforms of the 3D volumes that we need to compare. Typically, U and V are the reconstructed volumes inferred separately on two halves of the dataset: the method is said to perform well if the two reconstructed volumes U and V are similar, and the resolution of the method’s reconstruction is estimated as the best resolution for which U and V agree. The FSC is close to 1 when the two maps are close. This is typically the case for small k , as low-frequency signal is strong, but FSC generally decays to zero as the signal-to-noise decreases. The result is often plotted as a curve, with axis $x = k$. The final resolution of the recovered map corresponds to the maximum value of k such that $FSC(k) \geq 0.143$ — a criterion that is chosen to match resolution criteria used in X-ray crystallography. This is one of the most standard reference metrics in cryoEM. In fact, most methods (with the exception perhaps of atomVAE¹⁰) reviewed in the present paper use this metric to evaluate their recovered spatial resolution.

Fourier Shell Correlation between map and atomic model This is a variation on the previous metric and called the “map-to-model FSC”. In this case, the reported resolution is the maximum value of k such that the Fourier Shell Correlation is above 0.5. For instance, RELION¹⁸ reports, on top of two-halves FSCs, FSC calculations against available crystal structure as an additional objective indication of reconstruction quality.

Variants of the Root Mean Squared Error (RMSE). This method compares the root-mean-square deviation between 3D map. However, because images are random samples from the underlying volume, this metric needs to be adapted to compare distributions — which is done by using the Earth Mover (or Wasserstein) Distance: ground truth samples and predictions are aligned, their RMSD computed. An optimal assignment algorithm is then run to assign each ground truth sample to a corresponding prediction, and the reported RMSD is computed on this assignment. This is one of the metrics used by atomVAE¹⁰ to evaluate their algorithm.

Comparing Performances in Spatial Resolution: Lack of Common Benchmarks Despite the wealth of available metrics to quantify performance, reconstruction methods remain to this day hard to compare. Perhaps partly due to the relatively novel use of deep learning methods for cryo-EM molecular reconstruction, there exists no standard way of evaluating a method’s performance — or at least, not to the best of the authors’ knowledge. In fact, the objective quantitative assessment of these methods’ relative performance has yet to overcome three main hurdles:

- 1. Lack of common datasets:** There is unfortunately no “MNIST” or “Imagenet” of cryo-EM. Most methods thus resort to first evaluating their performance on synthetic data — thereby allowing them to control and assume known certain variables, such as pose for instance, and evaluate the accuracy of the reconstruction with one variable at a time. Experiments on real datasets are then typically ran, but the molecules chosen depend on the research group and are often too diverse to be compared across papers. Current methods are developed and tested on a wide range of synthetic and experimental datasets that differ in the nature of the biomolecule being imaged, the dataset size, image size and associated resolution — with very little overlap across methods (see Table 5). Beyond experimental data, there currently exists no standard cryo-EM simulator that could at least serve as benchmark to all current methods. Synthetic datasets vary in the realism of the image formation model used for simulation, *e.g.* the noise model or the signal-to-noise ratio that has been used. The important diversity within the characteristic of these evaluation datasets therefore makes the comparison of these methods a strenuous task.
- 2. Lack of unified metrics:** The systematic review of cryo-EM reconstruction methods is also plagued by a lack of established metrics. As detailed in the previous paragraph, there exists a few criteria that can be used to evaluate the resolution and success of the recovery. Yet, some approaches will prefer to evaluate their performance solely on synthetic datasets, and rely on the Mean Square Error (MSE) to compare the reconstruction to the ground-truth (synthetic) volumes (such as for instance atomVAE¹⁰). Other methods will favor using Fourier Shell Correlations between half-maps and/or crystal structures (such as for instance RELION¹⁸). Consequently, the diversity in reported metrics adds to the complexity of this comparison task.
- 3. Lack of reference code-bases:** Finally, these state-of-the-art methods are not necessarily easily accessible to the public, or are being implemented across different programming languages. Creating a codebase that would re-implement these methods for a proper evaluation would unfortunately represent a gigantic implementation effort. Currently, this lack of

¹We refer the reader to the excellent review by Singer *et al.*⁷ for a wider description of the topic.

| | Biomolecule | # of images | Image size | Data Type | Noise |
|-----------------------------|---|-----------------------|------------|--------------|--------|
| CryoDRGN ¹⁴ | Ribosome 80S (EMPIAR-10028) | 50,000 | 128 x 128 | Synthetic | No/Yes |
| | | 105,247 | 90 x 90 | Experimental | Yes |
| | Ribosome 50S (EMPIAR-10076) | 131,899 | 90 x 90 | Experimental | Yes |
| | Protein complex | 50,000 | 64 x 64 | Synthetic | N/A |
| CryoFold ²⁴ | Haemoglobin (PDB 5NII) | 50,000 | 128 x 128 | Synthetic | Yes |
| 3DFlex ²¹ | Tri-snRNP spliceosome (EMPIAR-10073) | 102,500 | 180 x 180 | Experimental | Yes |
| | TRPV1 ion-channel (EMPIAR-10059) | 200,000 | 128 x 128 | Experimental | Yes |
| CryoPoseNet ²³ | E.coli adenylate kinase (PDB 4AKE1) | 9,000 | 128 x 128 | Synthetic | No/Yes |
| E2GMM ²² | Ribosome 50S (EMPIAR-10076) | 124,900 | N/A | Experimental | Yes |
| | Precatalytic spliceosome (EMPIAR-10180) | 327,490 | N/A | Experimental | Yes |
| | SARS-CoV-2 spike protein (EMPIAR-10492) | 55,159 | N/A | Experimental | Yes |
| FSTdiff ²⁸ | GroEL-GroES protein | 40,000 | 128 x 128 | Synthetic | Yes |
| CryoVAEGAN ³¹ | Ribosome 80S (EMPIAR-10028) | 2, 544 | 128 x 128 | Synthetic | No |
| | | 5,119 - 8,278 - 4,917 | 128 x 128 | Experimental | Yes |
| atomVAE ¹⁰ | Aurora A Kinase (Simulated) | 63,000 | 64 x 64 | Synthetic | Yes |
| CryoGAN ²⁷ | β -galactosidase | 41,000 | 180 x 180 | Synthetic | Yes |
| | β -galactosidase (EMPIAR-10061) | 41,123 | 192 x 192 | Experimental | Yes |
| Multi-CryoGAN ³³ | Heat-shock protein Hsp90 | 100,000 | 32 x 32 | Synthetic | Yes |

Table 5. Summary of synthetic and experimental cryo-EM datasets on which the reconstruction methods have been tested. The light red background indicates methods that perform homogeneous reconstruction, and the light yellow background heterogeneous reconstructions.

unified coding repository poses a significant hurdle in the accessibility of these different methods, pushing methods to be developed somehow “agnostically” to one another.

Evaluating Conformation Heterogeneity: An Ill-Defined Problem Despite several hurdles in its deployment and practical use, the evaluation of spatial resolution is a well-defined problem. Evaluating conformation heterogeneity, on the other hand, is another — perhaps less well-defined – issue. To evaluate the methods ability to recover continuous heterogeneity for instance, methods like 3DFlex²¹ or CryoDRGN¹⁴ do a post-hoc analysis of the recovered latent space, showing the flexible deformation that are induced by sweeping through the space of possible z s and looking at deformations over trajectories. However, a proper objective way of measuring conformation heterogeneity remains to be established: there currently exists no standardized measure or gold-standard task to evaluate how well a method is able to capture it.

Consequently, in the remainder of this section, we propose instead to discuss models based on what can be inferred from the corresponding paper as well as our practical experience with these methods, focusing on two main criteria: (a) reproducibility and (b) tractability.

Reproducibility in Cryo-EM. The non-convex nature of the problem puts it at very high-risk of being non robust and sensitive to initialization — this is a phenomenon sometimes referred to as “Einstein from noise”³⁶ (also described in Singer *et al*⁷): the model is too heavily biased towards a reference template, and the optimization scheme fails to find the true signal in the data — “hallucinating” instead a solution close to the initialization point. Furthermore, the inference methods presented often make use of additional implementation tricks (e.g. warm-starting with a known shape), and specific regularization schemes (described in Appendix 4.2–4.4). The importance of implementation tricks and regularizations, and combinations thereof, is still ill-understood and would require an in-depth analysis. For instance, atomVAE¹⁰ reports that warm-starting their algorithm is essential in ensuring the success of the volume recovery: they suggest starting with initial phase of pose-only training, which, once realised, ensures that the further joint learning of poses and volume is successful. This hints towards a difficult optimization landscape for this method, and its great sensitivity to initial conditions. Moreover, each inference method (from Section 2) uses a different parameterization of the volume (from Section 1). It is thus challenging to disentangle the importance of each choice in the reconstruction pipeline.

Tractability. Finally, our last axis of comparison lies in the computational tractability and feasability of these methods. On this issue, there exists no proper benchmark or quantitative data. We thus propose to offer our own practical experience by-way of rule of thumb, with the hope of guiding the practitioner in correctly calibrating their expectations when running the different methods. Overall, cryo-EM volume reconstructions take a considerable amount of time. With datasets typically of more than 100GB, training times typically take up to 10 hours (including the required pre-processing steps) for methods like

RELION¹⁸ — that is, for a run that has little hyperparameter tuning compared to alternative deep learning methods. Newer methods like CryoDRGN¹⁴ hold great promise in terms of the reconstruction that they yield: however, from our practical perspective, this comes at the cost of huge memory requirements — sometimes requiring to set the latent dimension representing the conformation variable z to 1 for the method to run (which, arguably is detrimental to its huge potential). As such, such sophisticated methods can further benefit from gains in efficiency (both from the computational side and in terms of memory requirements). The efficient updating of a model’s parameters can thus be considered as a current computational bottleneck and offers an interesting avenue for future research.

4 Conclusion

This review provides a critical comparison of recent cryo-EM reconstruction methods that are based on deep generative modeling, focusing on explaining the choices that these pipelines make and their relative advantages or drawbacks. We have compared and contrasted existing methods through their parametrization of the volume, as well as through the optimization procedure chosen to infer parameters and hidden variables. While the use of amortized inference is crucial to make inference tractable in this high-data, high-dimensional setting, there seems to be much room for improvement and research on methods allowing both faster and better inference, perhaps through a richer class of priors — as amortized inference can translate into resolution loss, as explained by Punjani & Fleet²¹.

On a practical side, we note that recent methods suffer from a lack of current benchmarks which severely impedes their development. From our practical experience, beyond a unified benchmarking suite of data, we also highlight a severe need for the development of a diagnostic toolbox tailored to the analysis of cryo-EM data. Current methods rely on a set of choices and hyperparameters that raise a number of questions for the practitioner: have I chosen my hyperparameters adequately? Is this choice going to impact the accuracy of the recovery? Is there any physical or biological meaning or interpretation in the distance between the latent space of conformation variables? How does error on pose or CTF affect the rest of the volume recovery process? There seems to be a crucial need for more in-depth and systematic studies of these methods of (a) sensitivity to initialization and (b) robustness to error in the different components of the model.

To conclude, we therefore hope that this overview provide a clear unification of deep reconstruction methods, and a crisp description of the current hurdles that are impeding their development — which in turn could lead to a better understanding of their expected performances on real and synthetic datasets.

References

1. Ourmazd, A. Cryo-em, xfels and the structure conundrum in structural biology. *Nat. Methods* DOI: [10.1038/s41592-019-0587-4](https://doi.org/10.1038/s41592-019-0587-4) (2019).
2. Nakane, T. *et al.* Single-particle cryo-em at atomic resolution. *Nature* **587**, 152–156 (2020).
3. EMDB. Statistics. https://www.ebi.ac.uk/emdb/statistics/emdb_resolution_year (2022).
4. Kohl, H. & Reimer, L. *Transmission Electron Microscopy*. Springer Series in Optical Sciences.
5. Vulović, M. *et al.* Image formation modeling in cryo-electron microscopy. *J. Struct. Biol.* **183**, 19–32, DOI: <https://doi.org/10.1016/j.jsb.2013.05.008> (2013).
6. Scheres, S. H. RELION: Implementation of a Bayesian approach to cryo-EM structure determination. *J. Struct. Biol.* DOI: [10.1016/j.jsb.2012.09.006](https://doi.org/10.1016/j.jsb.2012.09.006) (2012).
7. Singer, A. & Sigworth, F. J. Computational methods for single-particle electron cryomicroscopy. *Annu. Rev. Biomed. Data Sci.* **3**, 163–190 (2020).
8. Kimanius, D., Forsberg, B. O., Scheres, S. H. & Lindahl, E. Accelerated cryo-EM structure determination with parallelisation using GPUS in RELION-2. *eLife* DOI: [10.7554/eLife.18722](https://doi.org/10.7554/eLife.18722) (2016).
9. Punjani, A., Rubinstein, J. L., Fleet, D. J. & Brubaker, M. A. CryoSPARC: Algorithms for rapid unsupervised cryo-EM structure determination. *Nat. Methods* DOI: [10.1038/nmeth.4169](https://doi.org/10.1038/nmeth.4169) (2017).
10. Rosenbaum, D. *et al.* Inferring a continuous distribution of atom coordinates from cryo-em images using vaes. *CoRR* [abs/2106.14108](https://arxiv.org/abs/2106.14108) (2021). [2106.14108](https://arxiv.org/abs/2106.14108).
11. Boyd, S., Boyd, S. P. & Vandenberghe, L. *Convex optimization* (Cambridge university press, 2004).
12. Bendory, T., Bartesaghi, A. & Singer, A. Single-particle cryo-electron microscopy: Mathematical theory, computational challenges, and opportunities. *IEEE signal processing magazine* **37**, 58–76 (2020).

13. Si, D. *et al.* Artificial intelligence advances for de novo molecular structure modeling in cryo-em. *arXiv preprint arXiv:2102.06125* (2021).
14. Zhong, E. D., Bepler, T., Davis, J. H. & Berger, B. Reconstructing continuously heterogeneous structures from single particle cryo-em with deep generative models. *arXiv preprint arXiv:1909.05215* (2019).
15. Ede, J. M. Deep learning in electron microscopy. *Mach. Learn. Sci. Technol.* **2**, 011004 (2021).
16. Wu, J.-G. *et al.* Machine learning for structure determination in single-particle cryo-electron microscopy: A systematic review. *IEEE Transactions on Neural Networks Learn. Syst.* 1–21, DOI: [10.1109/TNNLS.2021.3131325](https://doi.org/10.1109/TNNLS.2021.3131325) (2021).
17. Sharon, N., Kileel, J., Khoo, Y., Landa, B. & Singer, A. Method of moments for 3d single particle ab initio modeling with non-uniform distribution of viewing angles. *Inverse Probl.* **36**, 044003 (2020).
18. Scheres, S. H. A bayesian view on cryo-EM structure determination. *J. Mol. Biol.* DOI: [10.1016/j.jmb.2011.11.010](https://doi.org/10.1016/j.jmb.2011.11.010) (2012).
19. Scheres, S. H. Chapter eleven - classification of structural heterogeneity by maximum-likelihood methods. In Jensen, G. J. (ed.) *Cryo-EM, Part B: 3-D Reconstruction*, vol. 482 of *Methods in Enzymology*, 295–320, DOI: [https://doi.org/10.1016/S0076-6879\(10\)82012-9](https://doi.org/10.1016/S0076-6879(10)82012-9) (Academic Press, 2010).
20. Punjani, A. & Fleet, D. J. 3d variability analysis: Resolving continuous flexibility and discrete heterogeneity from single particle cryo-em. *J. Struct. Biol.* **213**, 107702, DOI: <https://doi.org/10.1016/j.jsb.2021.107702> (2021).
21. Punjani, A. & Fleet, D. J. 3d flexible refinement: Structure and motion of flexible proteins from cryo-em. *bioRxiv* DOI: [10.1101/2021.04.22.440893](https://doi.org/10.1101/2021.04.22.440893) (2021). <https://www.biorxiv.org/content/early/2021/04/22/2021.04.22.440893.full.pdf>.
22. Chen, M. & Ludtke, S. J. Deep learning-based mixed-dimensional gaussian mixture model for characterizing variability in cryo-em. *Nat. Methods* **18**, 930–936, DOI: [10.1038/s41592-021-01220-5](https://doi.org/10.1038/s41592-021-01220-5) (2021).
23. Nashed, Y. S. G. *et al.* End-to-end simultaneous learning of single-particle orientation and 3d map reconstruction from cryo-electron microscopy data (2021). [2107.02958](https://doi.org/10.4236/ojs.20212102958).
24. Zhong, E. D., Lerer, A., Davis, J. H. & Berger, B. Exploring generative atomic models in cryo-em reconstruction (2021). [2107.01331](https://doi.org/10.4236/ojs.2021210331).
25. Rose, Y. *et al.* Rcsb protein data bank: Architectural advances towards integrated searching and efficient access to macromolecular structure data from the pdb archive. *J. Mol. Biol.* **433**, 166704, DOI: <https://doi.org/10.1016/j.jmb.2020.11.003> (2021). Computation Resources for Molecular Biology.
26. AlQuraishi, M. Alphafold at casp13. *Bioinformatics* **35**, 4862–4865 (2019).
27. Gupta, H., McCann, M. T., Donati, L. & Unser, M. Cryogan: a new reconstruction paradigm for single-particle cryo-em via deep adversarial learning. *IEEE Transactions on Comput. Imaging* **7**, 759–774 (2021).
28. Ullrich, K., van den Berg, R., Brubaker, M. A., Fleet, D. J. & Welling, M. Differentiable probabilistic models of scientific imaging with the fourier slice theorem. *CoRR abs/1906.07582* (2019). [1906.07582](https://arxiv.org/abs/1906.07582).
29. Rohou, A. & Grigorieff, N. CTFFIND4: Fast and accurate defocus estimation from electron micrographs. *J. Struct. Biol.* DOI: [10.1016/j.jsb.2015.08.008](https://doi.org/10.1016/j.jsb.2015.08.008) (2015).
30. Dempster, A., Laird, N. & Rubin, D. B. Maximum Likelihood from Incomplete Data via the EM Algorithm. *J. Royal Stat. Soc. Ser. B (Methodological)* **39**, 1–38 (1977).
31. Miolane, N., Poitevin, F., Li, Y.-T. & Holmes, S. Estimation of orientation and camera parameters from cryo-electron microscopy images with variational autoencoders and generative adversarial networks. *CVPR conference, Work. on Comput. Vis. for Microsc. Image Analysis* (2019). [arXiv:1911.08121](https://arxiv.org/abs/1911.08121).
32. Goodfellow, I. J. *et al.* Generative Adversarial Nets. Tech. Rep. (2014).
33. Gupta, H., Phan, T. H., Yoo, J. & Unser, M. Multi-cryogan: Reconstruction of continuous conformations in cryo-em using generative adversarial networks. In *European Conference on Computer Vision*, 429–444 (Springer, 2020).
34. Gelfand, A. E. & Smith, A. F. M. Sampling-based approaches to calculating marginal densities. *J. Am. Stat. Assoc.* **85**, 398–409, DOI: [10.1080/01621459.1990.10476213](https://doi.org/10.1080/01621459.1990.10476213) (1990).
35. Duane, S., Kennedy, A., Pendleton, B. J. & Roweth, D. Hybrid monte carlo. *Phys. Lett. B* **195**, 216–222, DOI: [10.1016/0370-2693\(87\)91197-x](https://doi.org/10.1016/0370-2693(87)91197-x) (1987).
36. Henderson, R. Avoiding the pitfalls of single particle cryo-electron microscopy: Einstein from noise. *Proc. Natl. Acad. Sci.* **110**, 18037–18041 (2013).
37. Kingma, D. P. & Welling, M. Auto-Encoding Variational Bayes. In *Proceedings of the 2nd International Conference on Learning Representations (ICLR)* (2014).

Appendix A: Ab-initio vs Refinement Reconstructions

Section 1 established how cryo-EM methods target either homogenous or heterogeneous reconstruction, and how they can be reference-based or reference-free for the later. Here, we further split these methods into two categories, depending on whether they choose to operate *ab-initio* (ie. from scratch), or *by refinement* (ie, "warm-starting" the algorithm by using an existing and external volume estimate, such as for example a low resolution estimate).

From a statistical perspective, this nuance depends on whether or not we have a reasonable prior for the shape (refinement), or if we'd rather not bias the algorithm with external inputs (ab initio). *From a computational perspective*, this can be understood as an initialization choice: we can either proceed with random guess (ab-initio) or warm-start the optimization with a volume provided by another method. *From a biological perspective*, this boils down to how much we trust potential external reconstruction methods, and we think that they could be instrumental in recovering the structure.

Difference between Ab-initio/Refinement and Reference-Free/Reference-Based Ab-initio and refinement methods address the purpose of the reconstruction: whether we want a rough first estimate of the molecular shape, or we are interested in a high-resolution volume. They also differ in the initialization of the reconstruction: ab-initio operate with a initial volume that has been randomly initialized, while refinement have a blunt homogeneous reconstruction as the initial volume. Reference-free or reference-based methods address the parametrization of the molecular volume, which is represented as deviations from a template. We shall use the word "initial volume" to refer to the initialization in refinement methods, and "template volume" to refer to the reference volume used to parametrize the conformation landscape.

Ab-initio: Pros and Cons. Ab-initio methods are challenging: due to the highly non-convex, non-linear nature of the problem, these methods are at higher risk of inconsistencies, especially when targeting an heterogeneous reconstruction: solutions initialised at various random points might not necessarily converge to same point, and/or get stuck in local minima. By contrast, warm-starting the problem can yield faster, and more consistent convergence towards the solution. Warm-starting the solution might also increase consistency across recovered conformation, thereby preventing aberrations.

Refinement: Pros and Cons. Homogeneous reconstruction approaches can also benefit from warm-starting strategies: in RELION⁶ for instance, the hypothesised template is converted into Fourier coefficients, that are used in the initialisation part of the inference process. Refinement for homogeneous reconstruction holds several advantages, especially if the homogeneous reconstruction is either slow or very sensitive to initialization.

Yet, refinement also holds several disadvantages. This approach yields another fragmentation of the estimation pipeline, as it relies on a prior estimation of an initial "blunt" value by another pipeline. Moreover, as highlighted in the review of Bendory et al¹², it also exposes this solution to model bias: the structure recovered will be biased towards our initial prior — potentially hindering our ability to detect flaws in this original template or discovering new conformations. Finally, while the literature on the sensitivity of the methods to an erroneous warm-starting is also nonexistent, due to the challenges of this problem, we posit that this could severely hinder the performance of the algorithm.

Appendix B: Differentiability of the Generative Models

The methods described in this review leverage the ability to do inference with gradient-based optimization techniques. This requires the generative models to be differentiable — that is, to allow the differentiation of the loss associated with the output (an image) with respect to the parameters of the model through backpropagation. As explained in Section 1, the volume V (or \tilde{V} in Fourier space) can always be seen as a function from \mathbb{R}^3 to \mathbb{R} (or \mathbb{C}). The parameters defining this function depend on the choice of *parametrization*, as summarized in Table 6. To make sure that the model is differentiable, we need to ensure that all the operations required in the forward model presented by Equation 1 are differentiable. Table 6 summarizes the operations required to "rotate", "translate" and "project" the volume V and obtain the observed image. Those operations are:

- multiplication with a matrix $R \in \mathbb{R}^{3 \times 3}$,
- addition of a vector $\mathbf{t} \in \mathbb{R}^3$,
- application of an interpolation kernel,
- summation (if the volume is in image space),
- and analytical integration.

All these operations, if they involve the "differentiable parameters" can be differentiated through by backpropagation. As shown in Equation (1) (resp. Equation (2)) the last step of the generative model is the application of the PSF (resp. CTF) which is done with a convolution (resp. element-wise multiplication) with the projected volume. This last operation is also

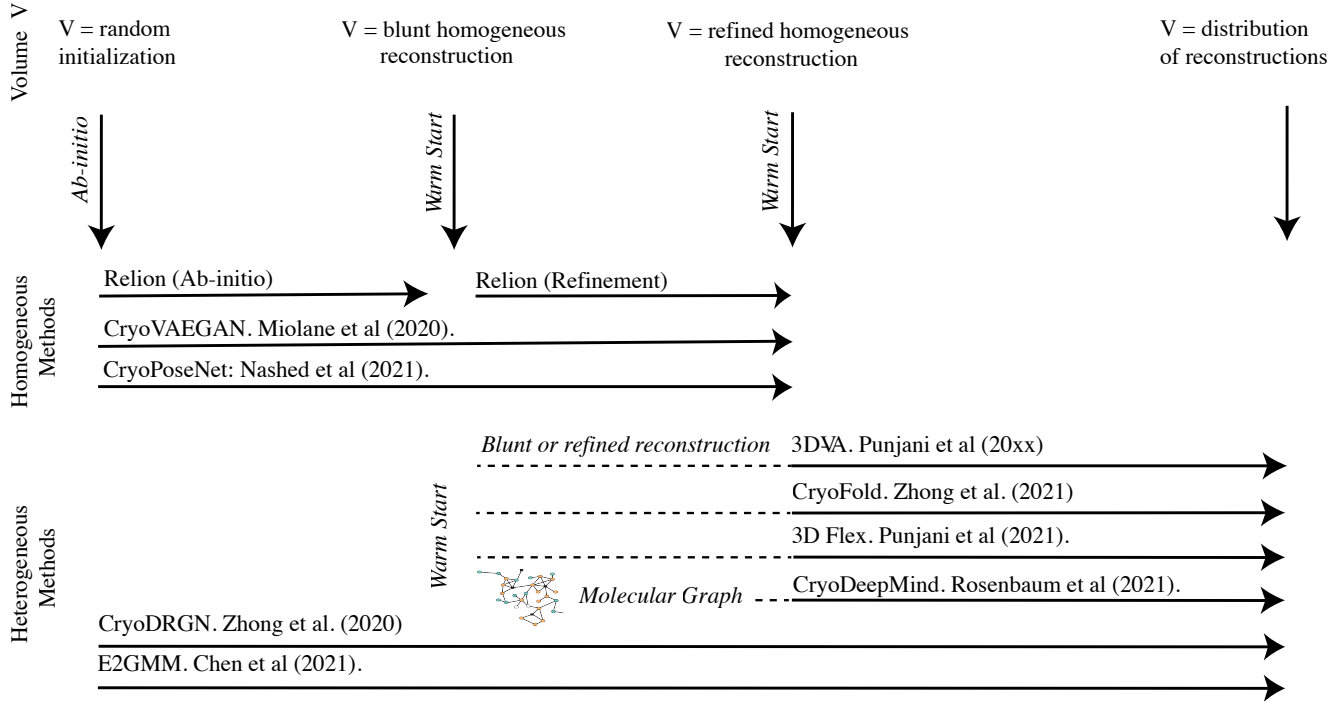


Figure 6. Works differentiated by the objective of the reconstruction (homogeneous/heterogeneous), and its initialization (ab-initio/warm-start).

differentiable, which in turn ensures that the whole generative model, transforming a volume V into an image (potentially in Fourier space), is differentiable.

| | Differentiable Parameters | Domain | Rotation Translation | Projection (in image space) |
|----------------------|---|---|---|--|
| Voxel Grid | $V(x)$ for $x \in \{1, \dots, D\}^3$ | $V : \{1, \dots, D\}^3$ With interpolation kernel, $\hat{V} : \mathbb{R}^3$, see ²⁸ | $\hat{x} = R^{-1}x - \mathbf{t}$ | $\sum_x \hat{V}(\hat{x})$ $\hat{V} : \mathbb{R}^3 \rightarrow \mathbb{R}$ |
| | Weights W | $V : \mathbb{R}^3$ | | $\sum_x V(\hat{x})$ |
| Mixture of Gaussians | A_j, c_j, σ_j | $V : \mathbb{R}^3$ With analytical integration, $\int V(., z) dz : \mathbb{R}^2$ | $c_j \rightarrow \hat{c}_j = R c_j + \mathbf{t}$ $V \rightarrow \hat{V}$ | $\int \hat{V}(y, z) dz$ for $y \in \mathbb{R}^2$ |

Table 6. Differentiable parameters and operations realized in the generative model, depending of the volume parametrization. V can be equivalently replace with \hat{V} in Fourier space. Using an interpolation kernel transforms the function V defined on $\{1, \dots, D\}^3$ into \hat{V} defined on \mathbb{R}^3 .

Appendix C: ELBO Computations

4.1 ELBO Computations

We provide the derivations leading to Equations (7)-(8) and the definition of the ELBO as a lower bound to the log-likelihood of the generative model. We start by expressing the observed log-likelihood of the model as:

$$\begin{aligned} L(X, \theta) &= \sum_{i=1}^n \log p(x_i | \theta) \\ &= \sum_{i=1}^n (\log p(x_i, h_i | \theta) - \log p(x_i, h_i | \theta) + \log p(x_i | \theta)) \\ &= \sum_{i=1}^n (\log p(x_i, h_i | \theta) - \log p(h_i | x_i, \theta)) \quad (\text{Bayes rule: } p(h_i | x_i, \theta) = \frac{p(x_i, h_i | \theta)}{p(x_i | \theta)}) \end{aligned}$$

In what follows, we drop the index i and associated sum for convenience. Consider any distribution $q(z)$. If we multiply both sides of the above equation by q , and integrate the z out, we get:

$$\begin{aligned} \int_z L(X, \theta) q(h) dh &= \int_h (\log p(x, h | \theta) - \log p(h | x, \theta)) q(h) dh \\ \implies L(X, \theta) &= \int_h (\log p(x, h | \theta) - \log p(h | x, \theta)) q(h) dh, \end{aligned}$$

since $L(X, \theta)$ does not depend on h . Now expanding the right hand side:

$$\begin{aligned} L(X, \theta) &= \int_h q(h) \log p(x, h | \theta) dh - \int_h q(h) \log p(h | x, \theta) dh \\ &= \int_h q(h) \log p(x, h | \theta) dh - \int_h q(h) \log \frac{p(h | x, \theta) q(h)}{q(h)} dh \\ &= \int_h q(h) \log p(x, h | \theta) dh - \int_h q(h) \log q(h) dh - \int_h q(h) \log \frac{p(h | x, \theta)}{q(h)} dh \\ &= \int_h q(h) \log p(x, h | \theta) dh - \int_h q(h) \log q(h) dh + KL(q(h) \parallel p(h | x, \theta)) \\ &= \mathbb{E}_q[\log(p_\theta(x, h))] - \int_h q(h) \log q(h) dh + KL(q(h) \parallel p(h | x, \theta)) \\ &= \mathbb{E}_q[\log(p_\theta(x, h))] + H(q) + KL(q(h) \parallel p(h | x, \theta)), \end{aligned}$$

by introducing the entropy of q as $H(q) = - \int_z q(z) \log q(z) dz$, and writing the KL-divergence between two distributions p_1 and p_2 as $KL(p_1 \parallel p_2) = \int p_1(x) \log(\frac{p_1(x)}{p_2(x)}) dx$.

In other words, for any distribution q on the latent variable H , the observed marginal likelihood $L(X, \theta)$ is the sum of three terms: (a) the expected log-likelihood, assuming that h has distribution q , (b) the Entropy of q , which can be understood of the amount of uncertainty in the estimation of h and (c) the KL-divergence between q and the true posterior $p(h | x, \theta)$, which measures how different these distributions are.

Note that, in the previous equations, terms (a) and (b) can be computed, but term (c) — the KL divergence between the proposed distribution q for h and the actual posterior distribution $p(h | x, \theta)$ is not unknown, because we do not know $p(h | x, \theta)$. However, because the KL-divergence is always non-negative, we know that:

$$L(X, \theta) \geq \mathbb{E}_q[\log(p_\theta(x, h))] + H(q).$$

Thus, introducing the ELBO term $\mathcal{L}(q, X, \theta) = \mathbb{E}_q[\log(p_\theta(x, h))] + H(q)$, we get:

$$L(X, \theta) = \mathcal{L}(q, X, \theta) + KL(q(h) \parallel p(h | x, \theta)). \quad (20)$$

which provides Equation (7) and the right hand side of Equation (8). Developping the ELBO term gives:

$$\begin{aligned} \mathcal{L}(q, X, \theta) &= \int_h q(h) \log p(x, h | \theta) dh - \int_h q(h) \log q(h) dh \\ &= \int_h q(h) \log p(x | h, \theta) dh + \int_h q(h) \log p(h | \theta) dh - \int_h q(h) \log q(h) dh \\ &= \int_h q(h) \log p(x | h, \theta) dh - KL(q(h) \parallel p(h | \theta)), \end{aligned}$$

which gives the left side of Equation (8).

4.2 EM as a Data Imputation Technique

The EM algorithm is often presented as a data imputation technique. Indeed, recall that in Equation (5), it would be easier to maximize the full log-likelihood $p_\theta(x_i, h_i)$ than the observed log-likelihood $L(X, \theta) = \log p_\theta(x_i)$, if only we knew the hidden variables h_i . The trick proposed by the EM is to "impute" (or fill in) the missing h_i values. To this end, instead of considering $L(X, \theta)$, we start with the "expected" log-likelihood with respect to any distribution q , defined as:

$$\mathbb{E}_{q_i}[\log p_\theta(x_i, h_i)] = \int_{h_i} \log p_\theta(x_i, h_i) q_i(h_i) dh_i.$$

In contrast to Equation (5), the log is now inside the integral, similarly to the second formulation of the ELBO in Equation (8). We simply have to find an appropriate distribution for q_i , for which we choose to be the posterior $q_i^{(t+1)} = p_{\theta^{(t)}}(h_i|x_i)$ given parameters computed in the current iteration t , as motivated by the tangent lower bounds described above. This can be considered an imputation step, since, for each value of h , we are filling in the h in the term $\log p_\theta(x, h)$ while associating with the corresponding this complete log-likelihood value with a different weight depending on $p_{\theta^{(t)}}(h|x)$. We get: $Q_i(\theta, \theta^{(t)}) = \int_{h_i} p_\theta(x_i, h_i) p_{\theta^{(t)}}(h_i|x_i) dh_i$, with $\theta^{(t)}$ the current estimate of the true θ at iteration t , and $Q(\theta, \theta^{(t)}) = \sum_{i=1}^n Q_i(\theta, \theta^{(t)})$. In this view, the EM algorithm starts with an initial guess $\theta^{(0)}$ of the parameter θ and performs two steps at each iteration t :

(a) Expectation step (E-step) : Given the current estimate $\theta^{(t-1)}$ of θ , we compute the expectation defining function Q_i :

$$\text{For each } i = 1, \dots, n: \quad Q_i(\theta, \theta^{(t-1)}) = \int_{h_i} p_\theta(x_i, h_i) p_{\theta^{(t-1)}}(h_i|x_i) dh_i. \quad (21)$$

(b) Maximization step (M-step) : Optimize $Q(\theta, \theta^{(t-1)})$ over θ to update the current estimate $\theta^{(t-1)}$ into $\theta^{(t)}$.

$$\theta^{(t)} = \arg \max_{\theta} Q(\theta, \theta^{(t-1)}) \quad (22)$$

These steps are iterated until convergence of $\theta^{(t)}$. In this setting, the tangent lower bound \mathcal{L}_i which is used as a proxy for $L(X, \theta)$ in the optimization over θ becomes the expected value Q_i of the complete log-likelihood $p_\theta(x_i, h_i)$ used as the proxy for $L(X, \theta)$ in the M-step. In fact, \mathcal{L}_i and Q_i only differ by the Entropy term $\int_{h_i} q_i(h_i) \log q_i(h_i) dh_i$ in Equation (8), *i.e.* a term that is independent of θ .

Appendix D: Details on (Variational) Autoencoders

Autoencoders (AEs) and variational autoencoders (VAEs) are the main realizations of the amortized variational inference approaches in the cryo-EM reconstruction literature. This appendix provides additional details to link the traditional presentations of the AEs and VAEs to the framework described in Section 2.

4.3 Autoencoders

An autoencoder traditionally aims to minimize the following loss function:

$$\ell(\theta, \xi) = \sum_{i=1}^n \|x_i - \hat{x}_i\|^2 = \sum_{i=1}^n \|x_i - f_{V_\theta}(h_i)\|^2 = \sum_{i=1}^n \|x_i - f_{V_\theta}(\text{Enc}_\xi(x_i))\|^2. \quad (23)$$

The output of the generative model f_{V_θ} is usually called a reconstruction and denoted $\hat{x}_i = f_{V_\theta}(h_i)$, while $\ell(\theta, \xi)$ is called the reconstruction loss. Note that the mean square error is used to quantify the reconstruction loss, but it can be replaced by other metrics. For example, the binary-cross entropy is a metric traditionally used to compare images x_i and \hat{x}_i . In this context, the goal is to perform the double minimization in θ and ξ such that:

$$\hat{\theta}, \hat{\xi} = \arg \min_{\theta, \xi} \ell(\theta, \xi). \quad (24)$$

By considering the decoder as latent variable model: $\hat{x}_i = f_{V_\theta}(h_i) + \varepsilon_i$ with ε_i a standard Gaussian noise, this loss corresponds to the negative log-likelihood, informed by the encoder.

To minimize this objective, the AE takes a gradient step at each iteration t , or backward pass through the network, such that:

(a) Encoder - Inference on latent variables h_i The encoder updates its weight ξ through a gradient step with learning rate α :

$$\xi^{(t)} = \xi^{(t-1)} - \alpha \nabla_\xi \ell(\theta, \xi). \quad (25)$$

(b) Decoder - Estimation of model's parameter θ The decoder updates its weight θ through a gradient step with learning rate α :

$$\theta^{(t)} = \theta^{(t-1)} - \alpha \nabla_\theta \ell(\theta, \xi). \quad (26)$$

We note that this gradient descent is usually performed via stochastic gradient descent, such that only a mini-batch of the data is considered at each iteration to compute ℓ , as opposed to the full dataset of n images.

4.4 Variational Autoencoders

A variational autoencoder traditionally aims to minimize the following loss function, which is the negative ELBO³⁷:

$$\mathcal{L}(\xi, \theta) = \sum_{i=1}^n \mathbb{E}_{q_\xi(h_i|X_i)} (\log(p_\theta(X_i|z)) + KL(q_\xi(h_i|X_i) || p(h_i))). \quad (27)$$

In this loss, the first term is called the reconstruction term, estimated with one Monte Carlo sample through the so-called "reparametrization trick", and is akin to the reconstruction loss of the AE. The second term is a KL divergence term that is called the regularization term, as it regularizes the posterior of the latent variable h_i by forcing it to be close to the prior $p(h_i)$ of h_i which is modeled by a standard Gaussian distribution.

We can rewrite this loss by using the functions Enc_ξ and Dec_θ , and assuming that the Monte Carlo sampling performed to compute the expectation happens by sampling a unique \tilde{h}_i through $q_\xi(h_i|X_i)$ which is the convention adopted in these architectures:

$$\mathcal{L}(\xi, \theta) = \sum_{i=1}^n \|x_i - \hat{x}_i\|^2 - KL(q_\xi(h_i|X_i) || p(h_i)) = \sum_{i=1}^n \|x_i - \text{Dec}_\theta(\text{Enc}_\xi(x_i))\|^2 - KL(q_{\text{Enc}_\xi}(h_i|X_i) || p(h_i)), \quad (28)$$

where the KL term has a closed form in terms of the output of the encoder, due to the fact that the q distribution belongs to a Gaussian family of diagonal covariance.

By realizing that the decoder only participates in the first term of the loss function, the VAE takes a gradient step at each iteration t , or backward pass through the network, such that:

(a) Encoder - Inference on latent variables h_i The encoder updates its weight ξ through a gradient step of learning rate α such that:

$$\xi^{(t)} = \xi^{(t-1)} - \alpha \nabla_\xi \mathcal{L}(\xi, \theta). \quad (29)$$

(b) Decoder - Estimation of model's parameter θ The decoder updates its weight θ through a gradient step with learning rate α :

$$\theta^{(t)} = \theta^{(t-1)} - \alpha \nabla_\theta \mathcal{L}(\xi, \theta) = \theta^{(t-1)} - \alpha \nabla_\theta \ell(\theta, \xi). \quad (30)$$

The main difference with the autoencoder is that the latent variable h_i is considered as a random variable, rather than a fixed deterministic value. That is, h_i is endowed with a parametric probability distribution represented by q — which is a Gaussian distribution with parameters output by the encoder, so that $h_i \sim N(\mu_\xi(X_i), \sigma_\xi^2(X_i))$ and $\text{Enc}_\xi(X_i) = (\mu_\xi(X_i), \sigma_\xi^2(X_i))$. Considering h_i s as random variables has been shown to lead superior reconstruction results over the autoencoder.

The VAE loss can be adapted as: $\mathcal{L}(\xi, \theta) = \sum_{i=1}^n \mathbb{E}_{q_\xi(z|X_i)} (\log(p(X_i|z)) + \beta KL(q_\xi(X_i|Z) || p(x)))$, where β is an additional hyperparameter introduced in β -VAE⁷. Traditional VAEs have $\beta = 1$, to ensure that the actual negative ELBO is minimized. Yet, to prevent pathological issues in the fitting of VAEs (including posterior collapse), recent work has shown that counterbalancing the reconstruction error with the KL divergence through a β could yield superior results.

In the cryo-EM implementations of the VAE architectures, the ELBO loss can be supplemented with additional terms that we name "structure losses" for now. We will explain it in the next appendix as it depends on the structure of the decoder (i.e. exact choice of generative model) chosen by the method.

Appendix E: Constraints

As described in the introduction and following the exposition by Scheres⁶ (2012), the molecule reconstruction problem is a difficult, highly non-linear inverse problem, which makes the parametrization of the shape and associated constraints particularly important. This parametrization amounts to impose structure on the desired reconstructed shapes — either by leveraging domain knowledge on the properties of molecular volumes, or by using external information to guide the reconstruction.

From a physics/biology perspective, this can be seen as a necessary enrichment of the cryo-EM data with either external assumptions and/or domain knowledge on the properties of the solution to ensure a more accurate recovery. *From a statistics perspective*, formulated this way, the problem rapidly takes on a Bayesian flavour, and the objective of this step is to find the right "prior" on the distribution of our latent variables. *From a computational perspective*, this corresponds to adding additional terms to the loss/objective defining the optimization problem, and effectively explains what we term "structure loss" in Section 2. We detail here the additional constraints that can equip the inference methods across the reconstruction algorithms.

4.5 Smoothness

Smoothness refers to the property by which a signal, or quantity of interest, varies with "no abrupt change" over continuous regions. As explained by Scheres (2012)⁶, "because macromolecules consist of atoms that are connected through chemical bonds, the scattering potential will vary smoothly in space, especially at less than atomic resolution." Smoothness of the

recovered scattering potential V thus appears to be a reasonable assumption, which is implemented in different ways depending on the parametrization chosen:

Smoothness of the 3D image. The smoothness assumption holds in image space as the image is a projection of the electron field — which is itself continuous. This smoothness is encoded by the normal distribution. This also calls to mind the "ridge penalty", a similar type of regularisation in statistics.

Smoothness of the Fourier coefficients. The smoothness of the 3D density map translates into smoothness over neighbouring Fourier coefficients. In a Bayesian pipeline, this is typically parametrized by assuming that these coefficients are sampled from a normal distribution. The RELION algorithm (Scheres⁶) is based on such a smoothness assumption. This prior is encoded by assuming independent Gaussian priors on the Fourier components of the signal: $V_l \sim N(0, \tau_l^2)$. Note here that the algorithm is not encouraging any other type of structure (e.g sparsity through spike-and-slab prior, etc).

Smoothness of the deformation field. 3DFlex²¹ directly exploits the knowledge that conformational variability of a protein is the result of physical processes that transport density over space. This means that mass and local geometry are preserved. As a result, this method implements a convection operator that outputs the deformation field. 3DFlex exploits prior knowledge of smoothness and local rigidity in the deformation field.

Smoothness of the function over 3D coordinates in Fourier domain. Cryo-DRGN¹⁴ and Cryo-Fold²⁴ represent the volume as the function $f : \Omega^3 \rightarrow \mathbb{R}$ over a 3D domain. In practice, this function is implemented by a neural network, which constrains it to be continuous, and possibly smooth if the activation functions used by the network are themselves smooth (sigmoids, for example).

4.6 Rigidity

Other constraints exploit physical properties and knowledge of the system to constrain the reconstruction. Specifically, due to the fact that the molecules studied in cryo-EM are frozen, we can assume that their conformational heterogeneity will not present large variations. As a result, we can assume that the molecular structure has some type of "rigidity". This is implemented in practice by refraining the variables describing the shape heterogeneity from varying excessively. Depending on the parametrization chosen to represent the volume heterogeneity, the rigidity constraint takes different forms:

Rigidity of the deformation field. The deformation field that parametrizes volume heterogeneity in 3D-Flex²¹ can be constrained to only generate "small" deformation, through a regularization term. This is integrated as a "structure loss" of the deep learning training procedure of 3D-Flex²¹.

Rigidity in (pseudo)-atoms coordinates. The (pseudo-) atoms coordinates that parametrize the volume heterogeneity in Cryo-Fold²⁴ are constrained to be close to a base conformation's coordinates, via an $L2$ penalization on the deformations. This forms the "structure loss" integrated in the objective function for the training procedure.

Rigidity in deviation from (pseudo)-atoms coordinates. Here, the volume is parametrized as a set of deviations of pseudo-atoms coordinates, compared to a base conformation, as in Cryo-DeepMind¹⁰. The rigidity of the molecular structure is thus enforced by adding a constraint that takes the form of a $L2$ regularization constraining the Δc_j to be small, and effectively forming the "structure loss" added to the optimization objective of this approach.

We also note that the methods that do not assume any heterogeneity in volumes V_i but rather model the volume as a unique possible conformation V , are essentially relying on the rigidity assumption, assuming that variations around V are not large.